



Effects of Thermal Damage on Strain Burst Mechanism for Brittle Rocks Under True-Triaxial Loading Conditions

Selahattin Akdag¹ · Murat Karakus¹ · Abbas Taheri¹ · Giang Nguyen¹ · He Manchao²

Received: 9 July 2017 / Accepted: 21 January 2018 / Published online: 17 February 2018
© Springer-Verlag GmbH Austria, part of Springer Nature 2018

Abstract

Strain burst is a common problem encountered in brittle rocks in deep, high-stress mining applications. Limited research focuses on the effects of temperature on the strain burst mechanism and the kinetic energies of rocks. This study aims to investigate the effects of thermal damage on the strain burst characteristics of brittle rocks under true-triaxial loading-unloading conditions using the acoustic emission (AE) and kinetic energy analyses. The time-domain and frequency-domain responses related to strain burst were studied, and the damage evolution was quantified by *b*-values, cumulative AE energy and events rates. The ejection velocities of the rock fragments from the free face of the granite specimens were used to calculate kinetic energies. The experimental results showed that thermal damage resulted in a delay in bursting but increased the bursting rate at ~ 95% of normalised stress level. This is believed to be due to the micro-cracks induced by temperature exposure, and thus the accumulated AE energy (also supported by cumulative AE counts) at the initial loading stage was reduced, causing a delay in bursting. The strain burst stress, initial rock fragment ejection velocity, and kinetic energy decreased from room temperature (25 °C) to 100 °C, whereas they resulted in a gradual rise from 100 to 150 °C demonstrating more intense strain burst behaviour.

Keywords Strain burst · Rock burst · True-triaxial loading · Thermal damage · Temperature · Acoustic emission · *b*-Value · Kinetic energy

1 Introduction

Rock burst is a typical unstable rock failure associated with the violent ejections of rock fragments from the free face/sidewall/roof of an underground excavation. Rock bursts can kill workers and cause severe injuries. They can also cause damage to mining and tunnelling structures that ceases the operations temporarily or permanently. Rock bursts are classified into three types: strain burst, fault-slip burst and pillar burst (Hedley 1992). Strain burst, which is the most prevalent type of rock burst, occurs due to the sudden release of stored strain energy within the rock mass when the induced major principal stress (σ_1) exceeds the rock mass strength (σ_{cm}). This type of detrimental failure process has been

observed in deep, hard rock mines and tunnels in different locations all around the world and is considered to be the biggest unsolved problem in deep underground excavations (He et al. 2016). Rock mass is in a state of stress equilibrium prior to any excavation ($\sigma_1 > \sigma_2 > \sigma_3$). Introducing an excavation in rock mass results in the redistribution of stresses around underground openings (see Fig. 1) and accumulation of elastic strain energy in the surrounding rock mass.

Additionally, rock mass surrounding underground excavations is vulnerable to the effects of high ground temperatures, especially at increasing depths. The physical and mechanical behaviours of the rock mass are influenced by the thermal effects, which threaten both the safety of the working environment and the efficiency of engineering projects (Chen et al. 2012; Liu and Xu 2013). For instance, a number of intense strain bursts occurred during the excavation of tunnels in the Jinping II Hydropower Station, which caused casualties and fatalities, damaged equipment and ceased operations due to the high geo-stress and high temperature (Zhang et al. 2012; Li et al. 2012; Feng et al. 2015). Understanding thermally induced damage in rock is,

✉ Murat Karakus
murat.karakus@adelaide.edu.au

¹ School of Civil, Environmental and Mining Engineering, The University of Adelaide, Adelaide, SA, Australia

² State Key Laboratory for GeoMechanics and Deep Underground Engineering, Beijing 100083, China

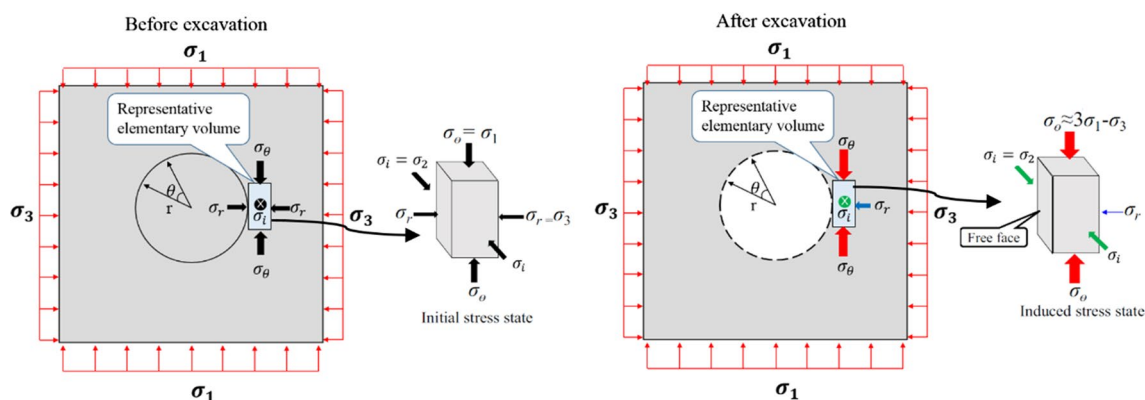


Fig. 1 Stress state change on the sidewall of an underground opening, and a representative elementary volume before and after excavation. (Modified from Su et al. 2017)

therefore, important for the safety and long-term stability of underground excavations. For this purpose, a realistic experimental testing system needs to be used for the assessment of thermal damage on the mechanism of strain burst.

Many researchers have investigated the influence of temperature on the mechanical and physical behaviour of rocks under uniaxial compression (Heuze 1983; Dwivedi et al. 2008; Sun et al. 2015), and under triaxial compression (Masri et al. 2014; Ding et al. 2016; Yao et al. 2016; Mohamadi and Wan 2016). Ding et al. (2016) studied damage evolution in sandstone after exposure to high-temperature treatment in unloading conditions and found that both peak ductile deformation and peak effective stress changed after a critical temperature level. Kong et al. (2016) investigated the AE characteristics and physical–mechanical properties of sandstone after high-temperature exposure under uniaxial compression conditions and found that AE parameters can be used for evaluating the thermal stability of rocks and for analysing crack development. These existing works clearly show considerable thermal effects on the mechanical behaviour of rocks (Xu and Karakus 2018) and the need to consider damage due to thermal effects in investigating strain burst in deep mining. In this sense, a true-triaxial condition that better reflects stress states in deep mining along with the effects of thermal damage on strain burst behaviour of rocks should be considered. However, to the best of our knowledge, all these features are either missing or not addressed at length in the previous works.

A considerable amount of research in the laboratory has been conducted to mimic the failure process of strain burst. These experiments have been mainly conducted under uniaxial compression (Nemat-Nasser and Horii 1982; Wang and Park 2001), conventional triaxial compression (Huang et al. 2001; Hua and You 2001) and true-triaxial compression (Mogi 1971; Atkinson and Ko 1973; Michelis 1985; Takahashi and Koide 1989; Wawersik et al. 1997; Haimson

and Chang 2000; Nasser et al. 2014; Feng et al. 2016). However, none of the aforementioned testing methods were able to realistically simulate the exact boundary conditions and stress paths for rocks during an excavation in which strain burst occurs. Hence, to characterise strain burst process in the laboratory, a novel true-triaxial strain burst testing system was developed by He et al. (2010) at the State Key Laboratory for Geomechanics and Deep Underground Engineering in Beijing, China. This hydraulic testing facility enables researchers to simulate the creation of an excavation by abruptly unloading σ_3 from one of the rectangular prism's surfaces that is exposed to air. Using this testing system, a considerable number of tests have been conducted on various types of rocks exposed to different stress paths to provide a better understanding of the mechanism of strain burst under true-triaxial loading/unloading conditions (He et al. 2010, 2012, Gong et al. 2012; Li et al. 2015). Few studies in the available literature have addressed the kinetic energy characteristics of strain burst failure. The influence of the unloading rate on strain burst behaviours of brittle rock under true-triaxial unloading conditions was studied by Zhao et al. (2014) concluding that the rock tends to strain burst more often when the unloading rate is high and the failure mode changes from strain burst to non-violent spalling as the unloading rate decreases. After creating a comprehensive database on the true-triaxial unloading tests, Akdag et al. (2017) discussed the influence of specimen dimensions on the bursting behaviour of rocks and indicated that the failure mode changes from strain bursting to local spalling when the height to width ratio of the rock sample is reduced from 2.5 to 1. For this reason and our focus on rock burst in the present study, we used all specimens with height to width ratio of 2.5. Su et al. (2017) investigated the influence of tunnel axis stress on strain burst by using modified true-triaxial rock burst system. The experimental results indicated that intensive strain burst is more likely to occur when the tunnel

axis stress is high. Table 1 summarises the true-triaxial loading and unloading tests to assess the failure characteristics of different rocks. However, the aforementioned studies did not consider the temperature influence on strain burst behaviours. Therefore, it is essential to investigate how strain burst mechanism is affected with high-temperature.

This paper investigates the influence of temperature on strain burst. A true-triaxial loading–unloading experimental set-up was used to replicate strain burst condition. In the following sections, the basic properties of the rock samples are described first. The strain burst testing methods and the experimental procedure are then introduced. This is followed by the analysis of the influence of temperature on strain burst stress and dynamic failure processes of strain burst. Subsequently, time-domain, frequency-domain and *b*-value analyses were conducted to systematically investigate the evolution of AE due to thermal damage influence on strain burst. Finally, the kinetic energies of the ejected rock fragments due to thermal damage are discussed.

2 Experimental Methodology

2.1 Rock Properties

The rock samples used in this study were collected from a borehole located in South Australia at a depth of 1020–1345 m. The collected rock was coarse-grained granite with weak to moderate alteration and occasional weak gneissic foliation. The grain size of this brittle granite rock

ranges from 0.5 to 3 mm and is composed of potassium feldspar, quartz and chlorite. Therefore, the diameter of the specimens was more than ten times bigger than the rock grain size required to satisfy ISRM recommendations (Fairhurst and Hudson 1999).

Uniaxial compression tests were performed on both cylindrical granite specimens that had a diameter of 42 mm, were subcored from 63-mm-diameter drill cores and were 100 mm long (Fairhurst and Hudson 1999). The tests were also performed on rectangular prism samples (125 mm × 50 mm × 25 mm). The granite specimens were loaded axially with an axial displacement rate of 0.1 mm/min, and LVDTs and strain gauges were attached to measure both axial and lateral strains. Rocks were also equipped with AE sensor to capture the cracking and damage behaviour during the tests (see Fig. 2). The test results and basic mechanical properties of the granite samples are listed in Table 2.

2.2 Experimental Procedure for Strain Burst Tests

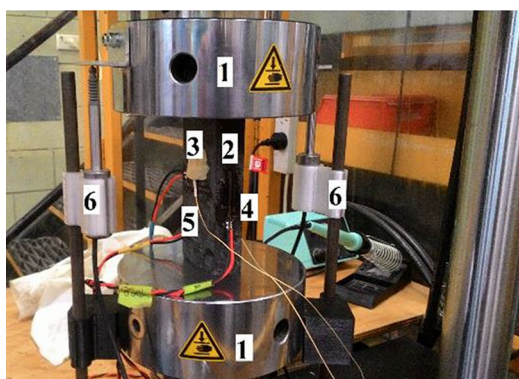
2.2.1 Sample Preparation and Strain Burst Testing System

A total of sixteen rectangular prism granite samples were prepared from the drill cores of 63 mm diameter for the strain burst tests (see Fig. 3a). Each sample size was approximately 125 mm × 50 mm × 25 mm. All six surfaces of the samples were carefully polished to minimise the end effect during loading. The samples' average flatness was 0.009 mm. Nine flatness measurements were taken from the

Table 1 Summary of true-triaxial loading and unloading tests to characterise the failure type of rocks

Loading type	Loading method	Specimen size (mm × mm × mm)	Rock type	Failure mode	References
Loading	(1) Apply $\sigma_1, \sigma_2, \sigma_3$	15 × 15 × 30	Dolomite	Fracturing and ductility	Mogi (1971)
	(2) Keep σ_2 and σ_3	50 × 50 × 100	Marble		Michelis (1985)
	(3) Increase σ_1	50 × 50 × 100	Sedimentary rocks		Takahashi and Koide (1989)
		57 × 57 × 125	Sandstone		Wawersik et al. (1997)
		19 × 19 × 38	Granite		Haimson and Chang (2000)
		80 × 80 × 80	Sandstone		Nasseri et al. (2014)
		50 × 50 × 100	Granite		Feng et al. (2016)
Unloading	(1) Apply $\sigma_1, \sigma_2, \sigma_3$	30 × 60 × 150	Limestone, granite, sandstone, marble	Rock burst	He et al. (2010, 2012)
	(2) Keep σ_2				
	(3) Unload σ_3	20 × 40 × 100	Marble	Spalling	Coli et al. (2010)
	(4) Increase σ_1	30 × 60 × 150	Marble	Rock burst and slabbing	Gong et al. (2012)
		30 × 60 × 150	Granite	Rock burst	Zhao et al. (2014)
		30 × 60 × 150	Granite	Rock burst	Zhao and Cai (2014)
		30 × 60 × 120	Granite	Slabbing	
		30 × 60 × 90	Granite	Shearing	
		100 × 100 × 100	Granite, sandstone, cement mortar	Splitting, Slabbing, Spalling	Li et al. (2015)
	100 × 100 × 200	Granite	Rock burst	Su et al. (2017)	

Fig. 2 Instrumentation of granite specimens for UCS tests



- 1: Instron 1342 testing machine**
- 2: Granite rock specimen**
- 3: AE sensor**
- 4: Axial strain gauge**
- 5: Lateral strain gauge**
- 6: LVDT**

Table 2 Mechanical properties of rectangular prism granite specimens for UCS (σ_{c2}) tests

Specimen number	Dimensions			Density (g/cm^3)	UCS, σ_{c2} (MPa)	Young's modulus, E (GPa)	Poisson's ratio, ν
	Height (mm)	Width (mm)	Thickness (mm)				
B1 #5	124.87	50.10	25.02	2.89	175.8	55.3	0.19
B1 #8	124.99	50.23	25.14	2.82	184.4	27.9	0.11
B3 #3	125.04	49.97	25.00	2.87	137.1	28.5	0.10

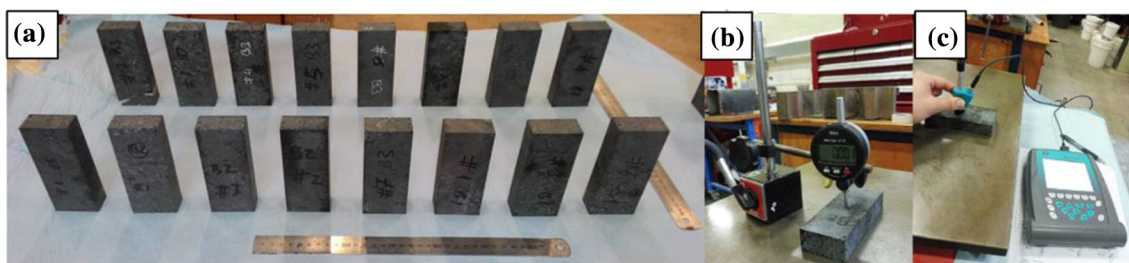


Fig. 3 **a** Overview of granite specimens, **b** flatness measurement by digital dial gauge, **c** hardness measurement via Equotip hardness tester

surfaces of each specimen using digital dial gauge. Sample hardness was measured with the Leeb rebound method, using an Equotip 3 hardness tester (see Fig. 3b, c). The Leeb number (L value) is used to express the hardness of the material, which can be used as an indicator of rock strength (Aoki and Matsukara 2008). The average Leeb hardness of the granite specimens used for this study was 746, and the average density was $2871 \text{ kg}/\text{m}^3$. The average P-wave velocity of the specimens before thermal damage was approximately 5764 m/s . All the granite specimens were divided into six groups (i.e. groups I, II, III, IV, V and VI) based on temperature. Specimens were then kept at room temperature of $25 \text{ }^\circ\text{C}$ (i.e. group I) or heated up to the following temperature levels of $50, 75, 100, 125$ and $150 \text{ }^\circ\text{C}$ (i.e. groups II, III, IV, V and VI, respectively).

The strain bursts tests were performed using the deep underground true-triaxial strain burst testing system developed by He et al. (2010) at the University of Mining and

Technology in Beijing, China. The strain burst test facility consists of a hydraulic controlling unit, a data acquisition system for stress and deformation, and also equipped with an AE monitoring system, a high-speed digital video camera system to monitor the instantaneous strain bursting process and linear variable differential transducers (LVDT) to measure the displacements during testing (see Fig. 4). To mimic and characterise the stress distribution near an excavation boundary in the laboratory, this testing system enables loading a rectangular rock specimen independently in three principal stress directions ($\sigma_1, \sigma_2, \sigma_3$) progressively to the predetermined in situ stress level, and suddenly removing σ_3 by dropping a rigid loading plate, while maintaining σ_2 constant and then increasing σ_1 until strain burst occurs (see Fig. 4d, e). The hydraulic loading unit has a maximum force capacity of 450 kN , which is used to apply vertical and horizontal loads on the six surfaces of a rectangular rock specimen. The data acquisition system is capable of recording 100,000

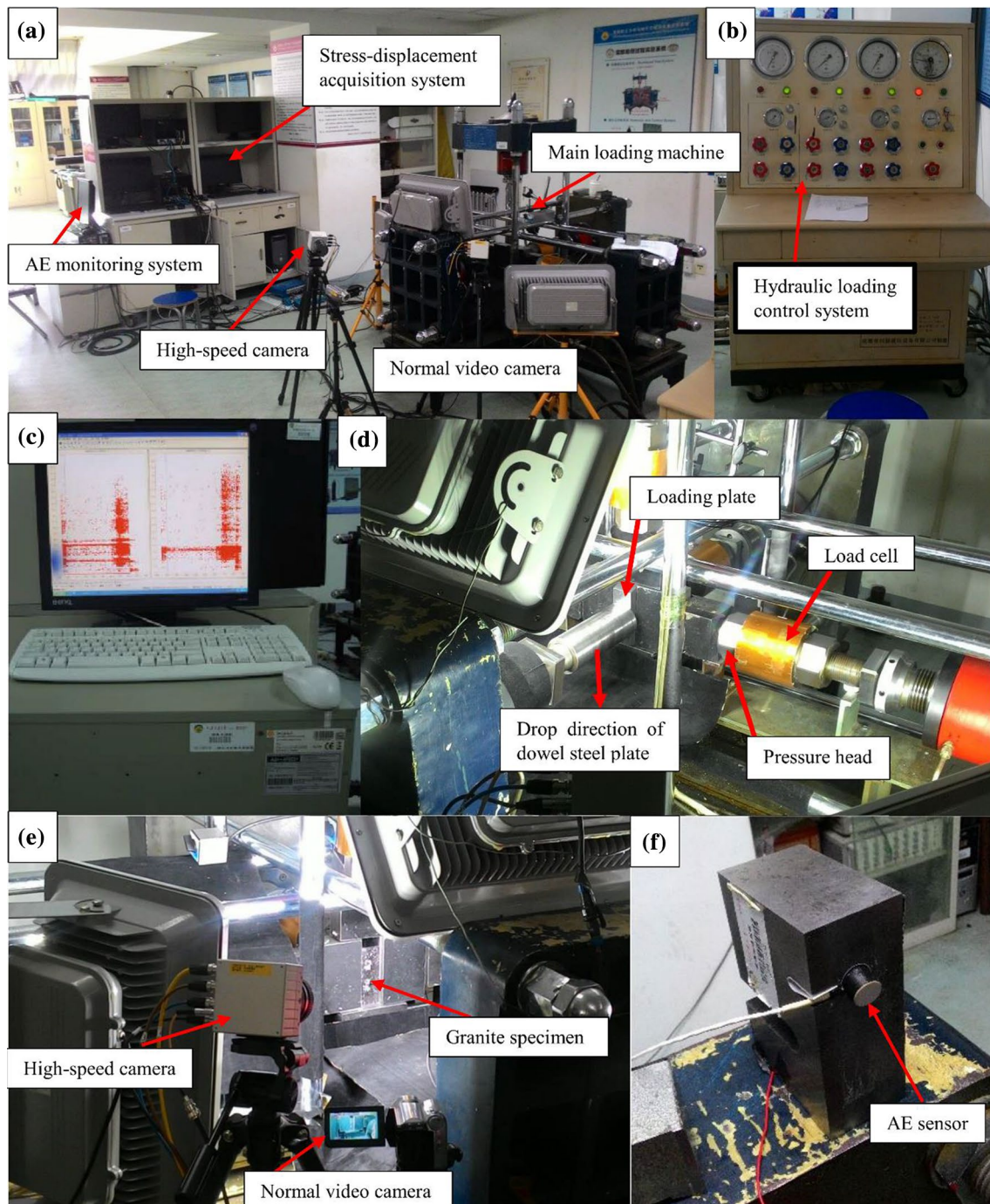


Fig. 4 Laboratory set-up for strain burst test: **a** the testing machine, data acquisition system and cameras, **b** independently controlled hydraulic loading system, **c** the AE monitoring system, **d** loading and

unloading steel plates, **e** granite specimen after unloading the plate from one face, **f** AE sensor position

data points per second (see Fig. 4a). The high-speed digital camera records at 1000 fps with a resolution of 1024×1024 pixels, which enables the capture of sudden cracking as well as the violent ejection of rock fragments (see Fig. 4e).

The AE technique is a useful, non-destructive testing method used to investigate the onset and evolution of

micro-cracking. It is also used to analyse the damage mechanism of rocks (Karakus et al. 2016). In the present study, we used two AE sensors with a diameter of 18 mm to investigate the AE characteristics of granite samples. The AE transducers (type WD, from the American Physical Acoustics Corp.) were attached to the lateral side of the rock specimens by

means of spring clips and adhesive tape to minimise friction between the specimen and the loading plate and to prevent sensor failure due to rock ejection (see Fig. 4f). A petroleum jelly was smeared on the sensors and the steel plates to ensure good acoustic coupling. The resonance frequency of the AE transducers was 125 kHz, associated with an operating frequency range from 100 kHz to 1 MHz. A PCI-2 AE system was used to monitor the damage within the granite specimens during strain burst tests, and the output voltage of the AE was amplified to 40 dB gain. The amplitude threshold for AE detection was set to 35 dB with an AE sampling rate of 10 msps (million samples per second) for each test.

2.2.2 Strain Burst Test

Granite specimens were first heated up to the target temperatures (25, 50, 75, 100, 125 and 150 °C) at a rate of 5 °C/min in a high-temperature furnace. Once the corresponding temperature was reached, the temperature was kept constant for about 12 h, to ensure the specimens were sufficiently heated. Finally, the granite specimens were allowed to cool down naturally to room temperature. Strain burst tests were then performed on the cooled granite samples.

Cai (2008) stated that it is significant to be able to capture the correct rock mass behaviour during excavations, because the actual stress path in a rock mass is complex and has an important role in the failure or damage process. Hence, accurate excavation responses depend on the unloading paths. The in situ stress test results were used as a guideline for determining the stress loading conditions used to simulate strain burst in the laboratory. Figure 5 plots the designed stress path and the applied loading–unloading directions on a rock specimen during strain burst testing. All surfaces of the rectangular prism granite specimen were loaded independently, in three principal stress directions.

The loads were progressively applied until all six surfaces reached the minimum principal stress. Subsequently, while the loads on two surfaces, where σ_3 was acting, were kept constant, the loads on the other four surfaces were increased simultaneously until they reached the intermediate principal stress level. Finally, while keeping the loads on the other lateral four surfaces constant, the load at the top surface was increased to the predetermined maximum principal stress level in two steps. Therefore, the in situ stress level of $\sigma_1/\sigma_2/\sigma_3 = 43/23/11$ MPa was reached and the loads were retained for about 5 min to make sure the stress was distributed uniformly. In order to mimic the stress redistribution and concentration after an excavation, σ_3 was removed quickly with an unloading rate of around 17 MPa/s while σ_2 was kept constant. Then to generate a strain burst, σ_1 was increased at a constant rate of 0.25 MPa/s until strain burst occurred. Meanwhile, when unloading of σ_3 began, recording of the high-speed digital video camera was started to capture the strain burst process.

3 Evaluation of the Experimental Results

3.1 Influence of Thermal Damage on Strain Burst Stress

The principal stresses applied to the granite samples just before unloading, and at failure, under various temperature conditions are summarised in Table 3. The table shows the ratios of major principal stress σ_1 , the sum of major and intermediate principal stresses and the deviatoric stress to the UCS (σ_{c1} , σ_{c2}) of both cylindrical and rectangular prism granite specimens. Note that σ_{c1} is the average value of UCS of cylindrical granite specimens (42 mm \times 100 mm), which is equal to 155 MPa and σ_{c2}

Fig. 5 Designed loading–unloading stress path and illustration of stress conditions on rock specimen for strain burst tests

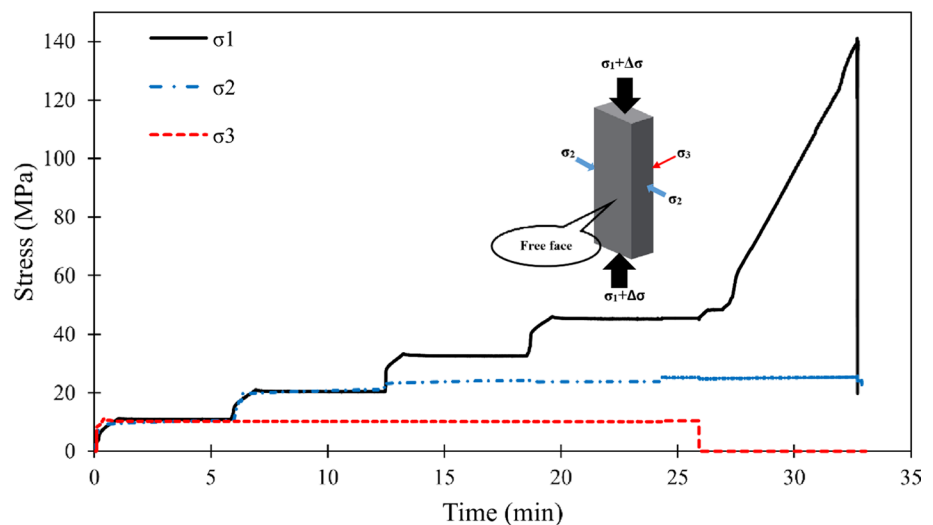


Table 3 Principal stresses just before unloading and at strain burst of granite specimens with different temperature conditions

Specimen	Temperature (°C)	Critical principal stresses before unloading			Critical principal stresses at strain burst			$\frac{\sigma_1}{\sigma_{c1}}$	$\frac{\sigma_1+\sigma_2}{\sigma_{c1}}$	$\frac{\sigma_1-\sigma_2}{\sigma_{c1}}$	$\frac{\sigma_1}{\sigma_{c2}}$	$\frac{\sigma_1+\sigma_2}{\sigma_{c2}}$	$\frac{\sigma_1-\sigma_2}{\sigma_{c2}}$
		σ_1 (MPa)	σ_2 (MPa)	σ_3 (MPa)	σ_1 (MPa)	σ_2 (MPa)	σ_3 (MPa)						
B1 #1	25	42.96	25.30	10.85	259.21	26.53	0	1.67	1.84	1.50	1.44	1.59	1.29
B1 #2		43.24	24.47	10.63	232.53	23.71	0	1.50	1.65	1.35	1.29	1.42	1.16
B2 #1	50	45.54	24.99	10.46	141.01	25.42	0	0.91	1.07	0.75	0.78	0.92	0.64
B2 #2		45.76	23.79	10.65	191.52	23.91	0	1.24	1.39	1.08	1.06	1.20	0.93
B2 #3		43.13	23.82	10.82	289.23	25.90	0	1.87	2.03	1.70	1.61	1.75	1.46
B1 #3	75	45.43	23.59	10.81	157.95	24.07	0	1.02	1.17	0.86	0.88	1.01	0.74
B1 #4		43.74	24.35	10.42	175.29	23.27	0	1.13	1.28	0.98	0.97	1.10	0.84
B1 #6	100	43.65	24.91	10.21	164.66	24.65	0	1.06	1.22	0.90	0.91	1.05	0.78
B1 #7		42.75	23.90	11.02	143.19	23.93	0	0.92	1.08	0.77	0.80	0.93	0.66
B3 #1	125	42.71	25.09	10.92	101.15	24.84	0	0.65	0.81	0.49	0.56	0.70	0.42
B3 #2		45.07	24.96	10.87	172.04	25.66	0	1.11	1.28	0.94	0.96	1.10	0.81
B3 #4		43.91	24.70	10.94	151.71	24.32	0	0.98	1.14	0.82	0.84	0.98	0.71
B3 #5	150	42.49	24.54	11.25	148.97	24.86	0	0.96	1.12	0.80	0.83	0.97	0.69
B3 #6		43.82	23.58	10.99	164.21	22.45	0	1.06	1.20	0.91	0.91	1.04	0.79
B3 #7		44.50	24.87	10.98	258.97	26.67	0	1.67	1.84	1.50	1.44	1.59	1.29
B3 #8		41.52	24.56	10.92	197.60	24.73	0	1.27	1.43	1.12	1.10	1.24	0.96

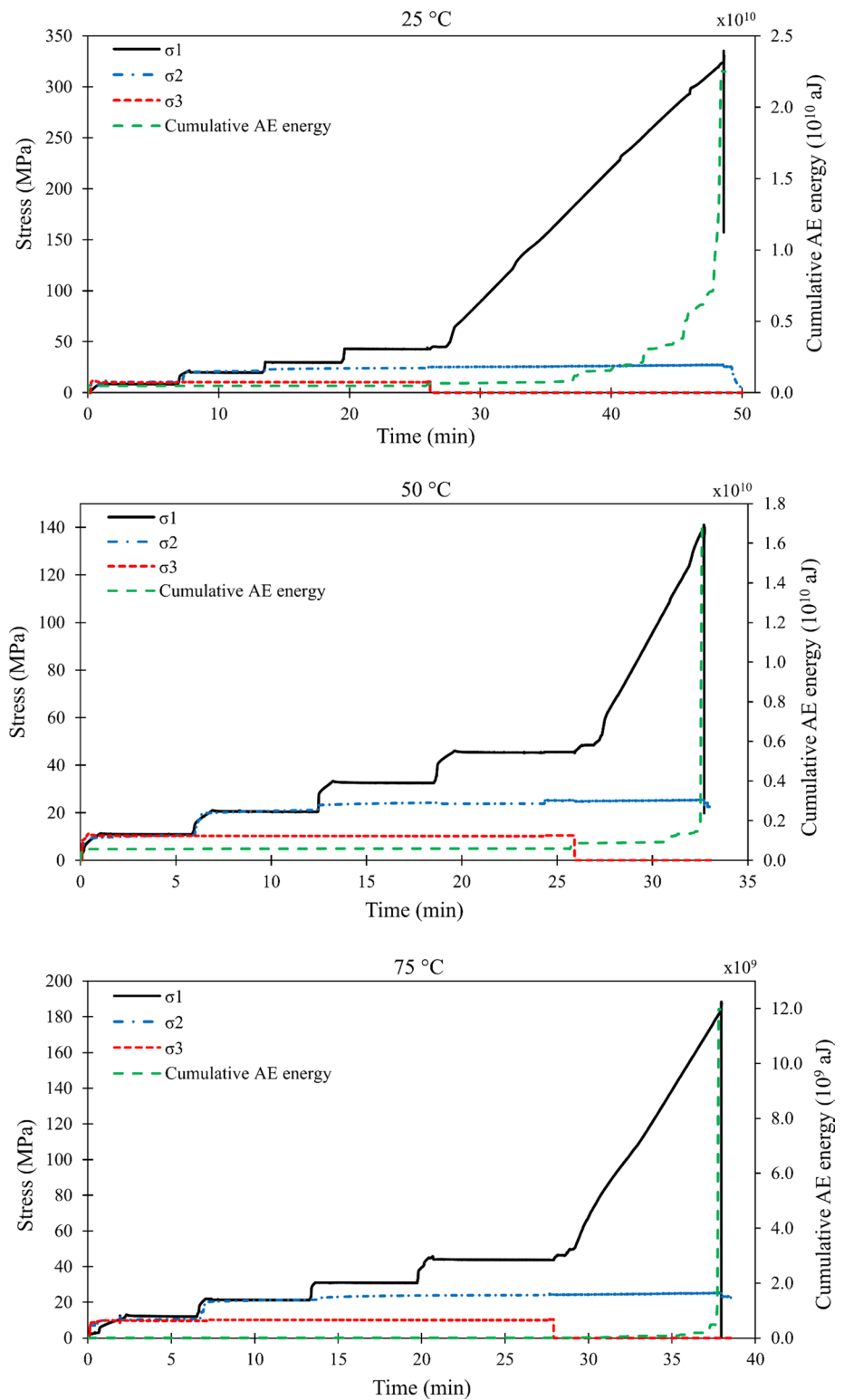
corresponds to the average UCS value of rectangular prism specimens (25 mm × 50 mm × 125 mm), which is 180 MPa. The major principal stress σ_1 at failure varies in the range of 0.65–1.87 times σ_{c1} and 0.56–1.61 times σ_{c2} . It is also shown that the ratio of deviatoric stress of σ_1 and σ_2 to σ_{c1} and σ_{c2} is between 0.49–1.70 and 0.42–1.46, respectively. The ratios indicated in Table 3 can be used as indicators of strain burst occurrence by comparing them to the rock burst criteria based on strength theory. Figure 6 presents the actual stress paths and cumulative AE energy, which was calculated after AE analysis, of the granite specimens from each group under different temperature conditions. As the testing system was not servo-controlled, you will see in Table 3 some discrepancies can be conserved between the recorded principal stresses and the designed values during the loading–unloading processes. Note that only one representative result from each group is presented in Fig. 6 to avoid providing similar results. However, the variations in strain burst stress and cumulative AE energy are shown separately in Figs. 8 and 12a, to represent the whole dataset.

It can be observed that the cumulative AE energy for the six granite specimens shows similar evolutionary characteristics to the initial stress state, unloading and failure. The evolution process of cumulative AE energy can be divided into three typical periods. At the initial loading period, a sharp increase occurred due to seating, loading adjustment and the natural compaction of micro-cracks and voids. Relatively low AE activities were observed in the second stage, showing that the rock samples went into elastic deformation.

When σ_3 was removed, the stepwise increase in the cumulative AE energy can be seen, and then a gradual increase due to new stable micro-crack generation and coalescence. In the final period, we observed a rapid increase in AE activities, due to the developments of unstable macro-cracks, and coalescence until failure (see Fig. 6).

Profiles of the six surfaces of the granite specimen B1#1 after strain burst testing are presented as the representative results in Fig. 7. The orientation of the tensile fractures near the free face is almost parallel to σ_1 . It can be seen from Fig. 8 that strain burst stress changes with temperature. Strain burst stresses were normalised with respect to the average UCS value of rectangular prism specimens (25 mm × 50 mm × 125 mm) as it would be more consistent to compare the results of UCS from rectangular prism than the cylindrical ones. Note that strain burst stress refers to the stress level where the first rock fragments were ejected from the free face of the specimens. As shown in Fig. 8, the strain burst stress decreased when the temperature increased from 25 to 100 °C since the thermally induced microstructures may lead to the degradation of mechanical strength (Sirdesai et al. 2017). For the granite specimens treated with temperatures 50, 75 and 100 °C, the average strain burst stress decreased by 15.7, 32.2 and 44.6%, respectively, in reference to the samples at room temperature 25 °C. The average normalised strain burst stress level also decreased from 1.37 to 0.76. When the temperature was increased from 100 up to 150 °C, strain burst stress showed a gradual increase. The normalised strain burst stress varied from 0.76 to 1.15. We

Fig. 6 Actual stress paths and cumulative AE energy of the granite rock specimens under different temperature conditions

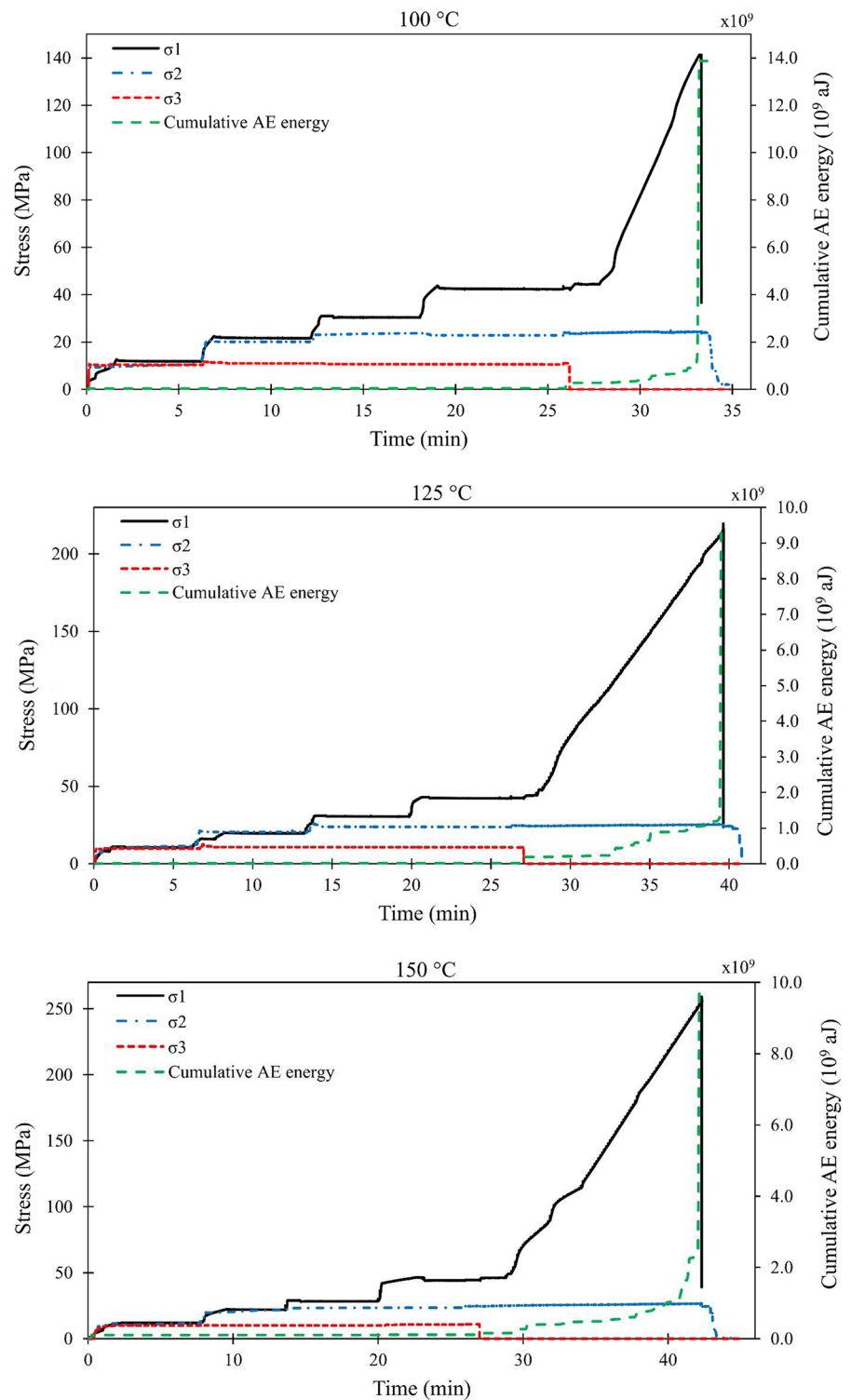


believe that this can be attributed to the thermal expansion of mineral grains by temperature which improved the compactness of the rocks. This observation is consistent with those stated by Yin et al. (2012) who investigated the effect of thermal treatment on granite samples.

3.2 Observations on the Influence of Thermal Damage on Strain Burst Behaviour

In order to capture the failure processes of the granite samples induced by the different temperature conditions,

Fig. 6 (continued)



a high-speed camera was used. Using a frame rate of 1000 f/s (frames per second), we observed the dynamic failure characteristics of the tested samples, including the crack growth and fragment ejection. A series of images for the samples were captured to investigate the influence of temperature on the rock failure process. These are

presented in Fig. 9. The numbers at the bottom-left corner of the snapshots indicate time in h:m:s.ms. It should be noted that regardless of the temperature, strain bursts occurred in all specimens. A common strain burst development process for all of the specimens was as follows: splitting of rock into rock plates, bending of the rock plates,

Fig. 7 Six surfaces for granite specimen B1#1 after strain burst test

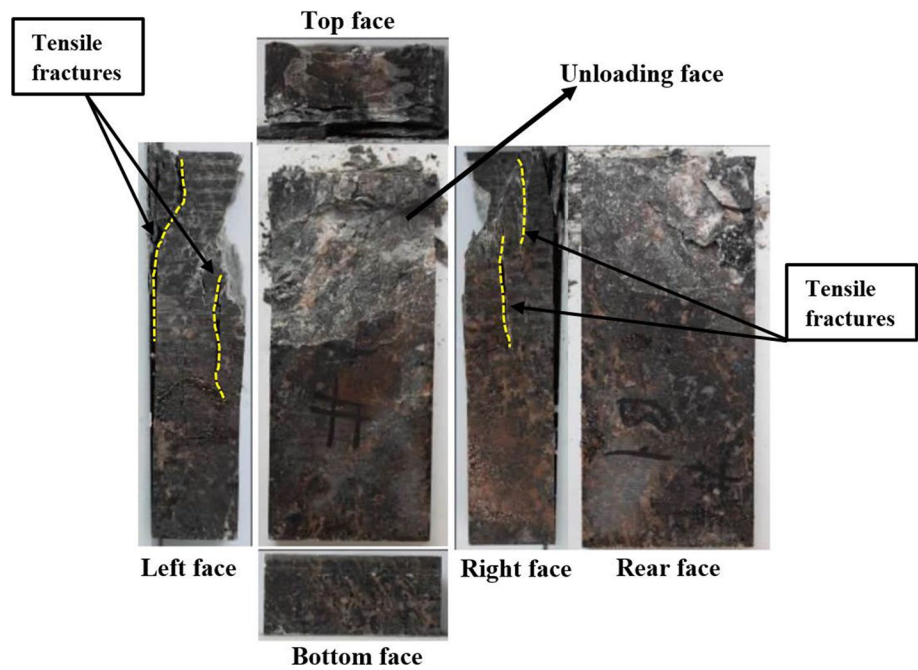
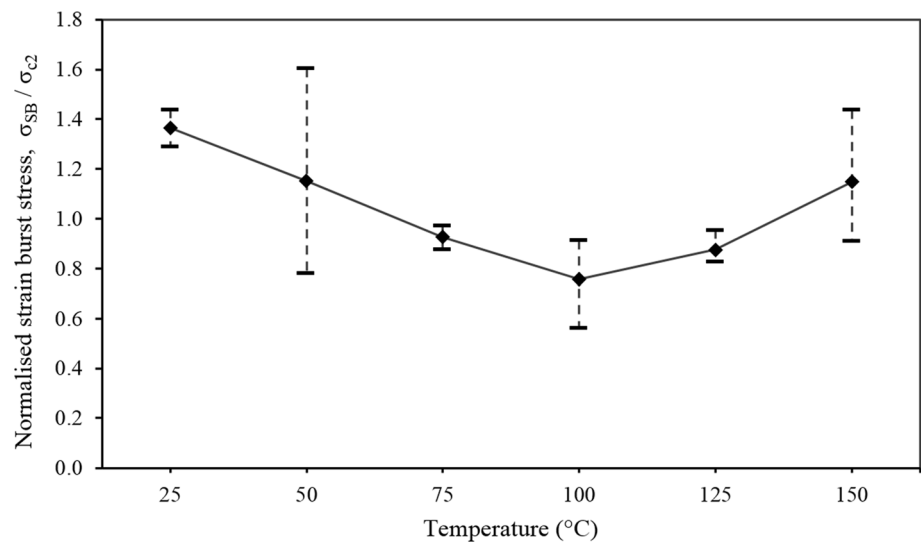


Fig. 8 Influence of temperature in strain burst stress



ejection of rock fragments and rock plates at high speeds accompanied by a loud explosion sound after the rock plates break off. It can be observed from Fig. 9 that the intensity of the strain burst differs moderately in different temperature conditions. For granite specimen tested at the temperature of 25 °C, (see Fig. 9a), where the specimen did not experience any thermal damage, the upper part of the free face split into rock plates, and small fragments were ejected at high speed. After the upper rock plate broke off, a large number of fragments and rock plates were suddenly ejected outward, and this activity was associated with a loud sound. The final strain burst pit area was around half of the whole free surface of the specimen and

tensile cracks near the free face occurred parallel to σ_1 on both lateral sides. When the temperature was increased up to 100 °C (see Fig. 9d), strain burst further became less violent. This may be caused by the thermal damage due to the deteriorated bonding among mineral grains that rendered the rock relatively weaker after temperature. Tensile cracks are observable at the free face of the sample. As the temperature increased from 100 to 150 °C, more violent strain burst characteristics were observed, as shown in Fig. 9e, f. This gradual change can be attributed to the compaction of the rock samples due to the closure of pre-existing micro-cracks (Kumari et al. 2017).

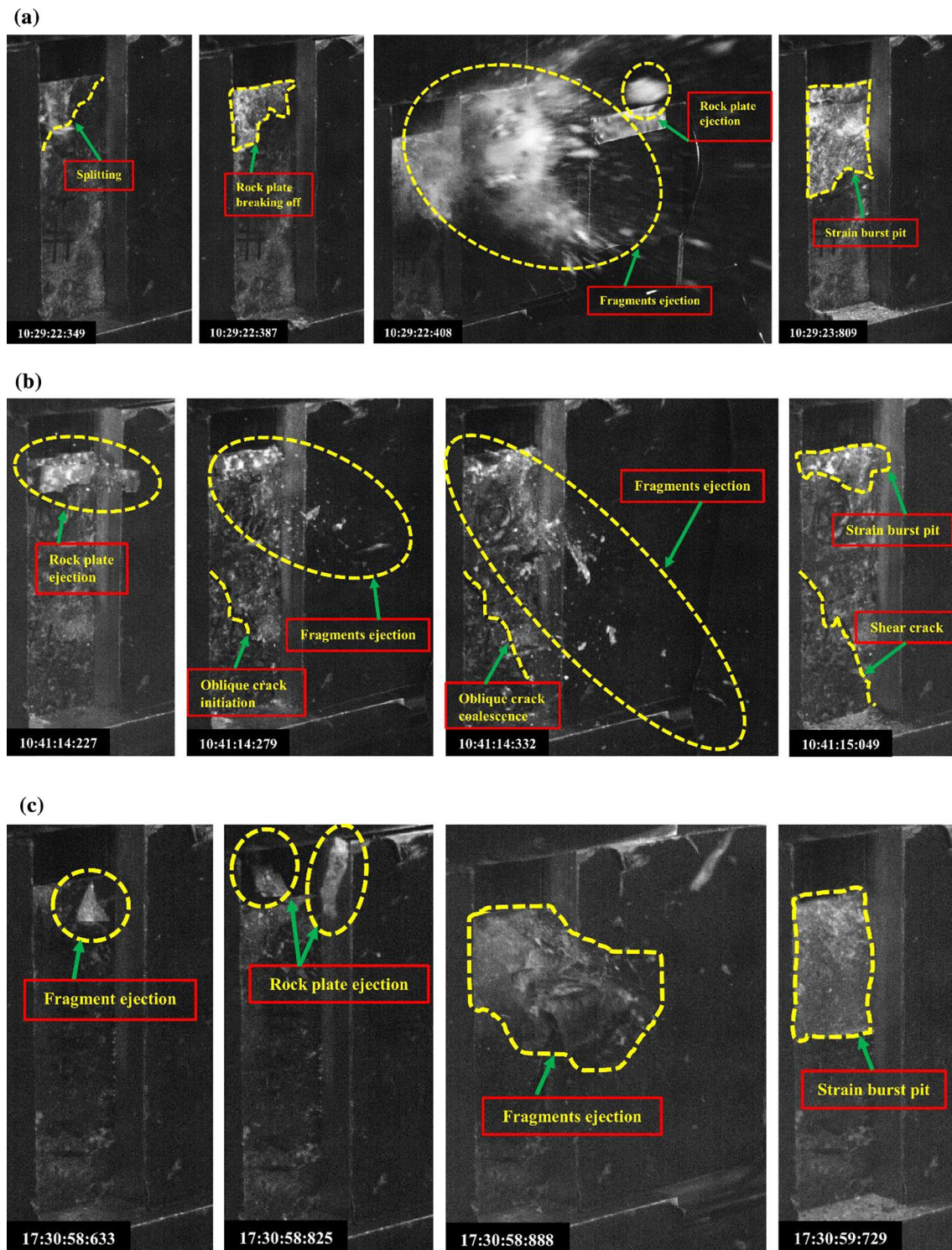


Fig. 9 Rock failure process of the granite specimens treated with different temperatures captured by the high-speed camera: **a** $T = 25\text{ }^{\circ}\text{C}$; **b** $T = 50\text{ }^{\circ}\text{C}$; **c** $T = 75\text{ }^{\circ}\text{C}$; **d** $T = 100\text{ }^{\circ}\text{C}$; **e** $T = 125\text{ }^{\circ}\text{C}$; **f** $T = 150\text{ }^{\circ}\text{C}$

3.3 AE Analysis for Thermal Damage Assessment

It is well understood that rock failure is accompanied by the release of energy. Elastic waves propagating from a source

within a material by the rapid release of localised energy can be defined as an acoustic emission. The AE method has been widely used to investigate brittle rock failure, and to quantify rock damage in many engineering applications (Lockner

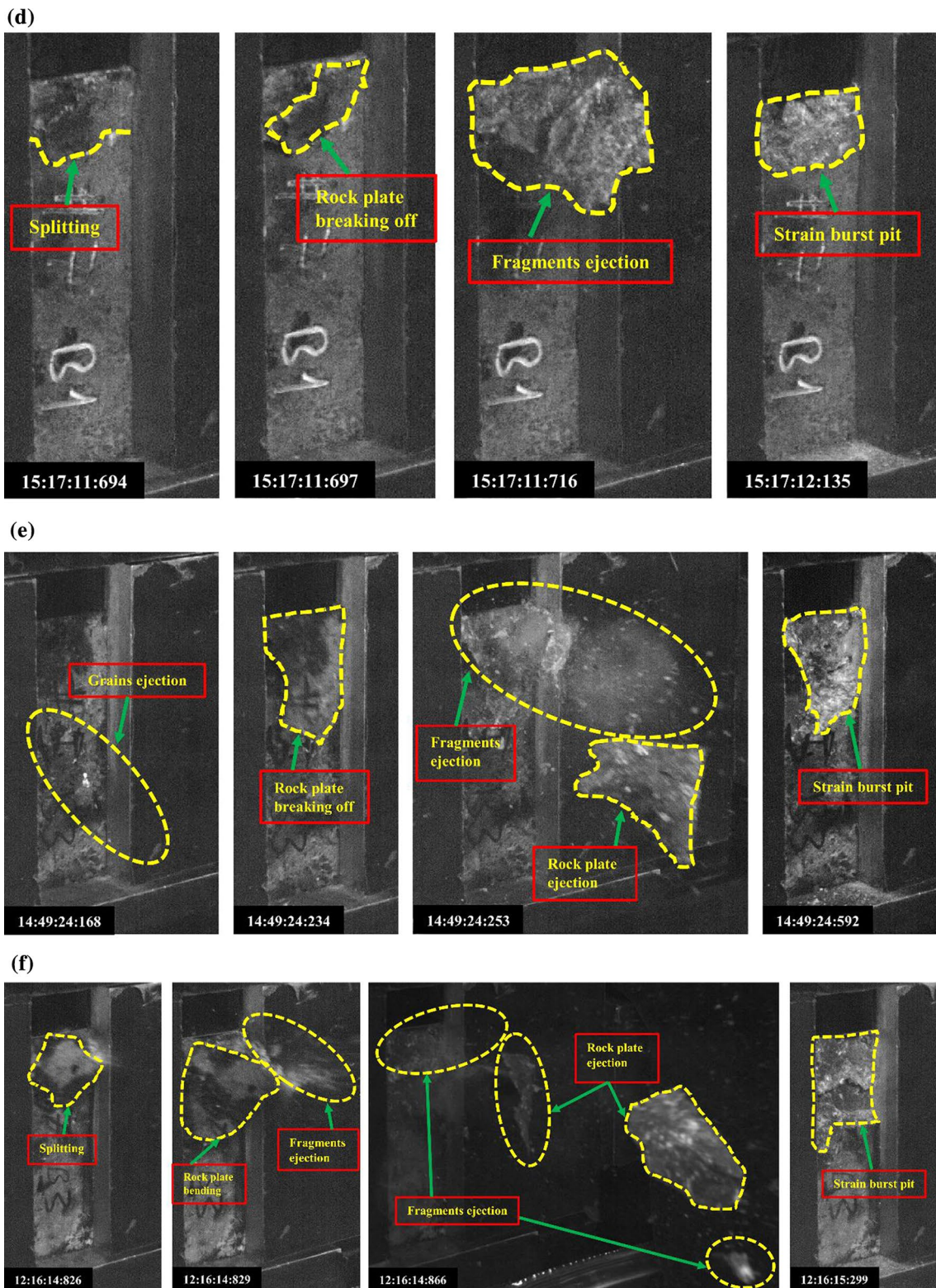


Fig. 9 (continued)

1993; Grosse and Ohtsu 2008; Nicksiar and Martin 2012; Carpinteri et al. 2013; Zhao et al. 2015; Karakus et al. 2016). As shown in Fig. 4, the AE technique was used to monitor the evolution of damage inside the granite samples at various temperatures.

3.3.1 Time-Domain Analysis

AE parameters such as counts, hits, energy, amplitude and frequency were obtained from the AE monitoring system, and the fracturing processes of strain burst under different temperature conditions were investigated. While the number of cracks is manifested by AE hits, the magnitude of the micro-cracking is related to the AE energy. Cumulative AE energy was therefore used to assess the energy release characteristics of the granite specimens subjected to various temperatures under true-triaxial unloading conditions.

Figure 6 illustrates the evolution of cumulative AE energies of the samples. It can be seen that although temperature conditions were different, the evolution features of cumulative AE energy for the six specimens underwent a similar trend from the beginning of loading until strain burst. Based on the cumulative AE energy characteristics, the evolution of AE behaviour was divided into three typical stages, i.e. the AE quiet linear elastic deformation stage, the AE growth stage and the AE active strain burst stage. Figures 10a and 11a depict the rate and cumulative plots of the AE energy and hits versus the time and also corresponding normalised strain burst stress in which the three deformation stages of strain burst are also demonstrated. The damage caused by temperature was quantified by changes in AE signal characteristics. Therefore, thermal damage for strain burst (D_{SB}) can be calculated for the granite specimens treated with different temperature conditions by using Eq. 1:

Fig. 10 Plots of **a** AE energy rate and **b** cumulative AE energy and damage evolution by AE energy versus normalised strain burst peak stress at corresponding stages shown in part a for the rock at temperature of 25 °C

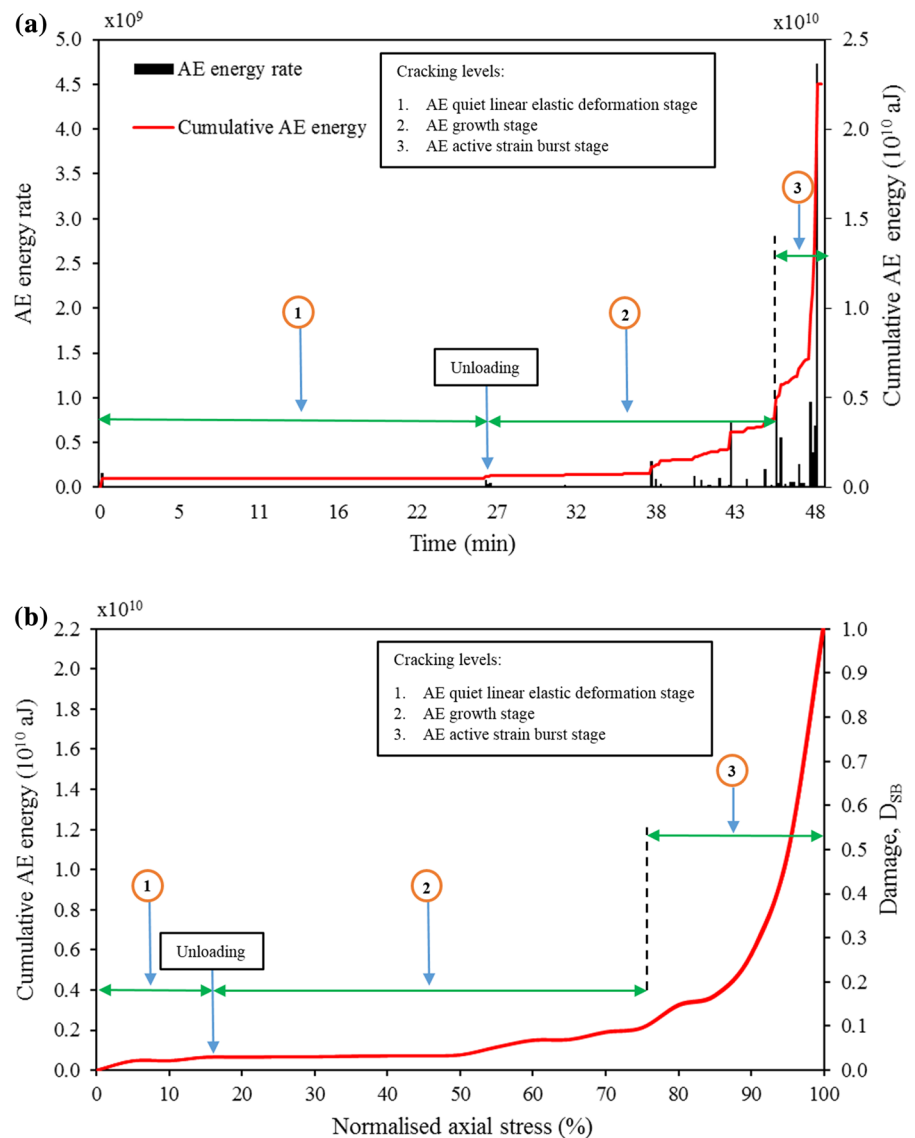
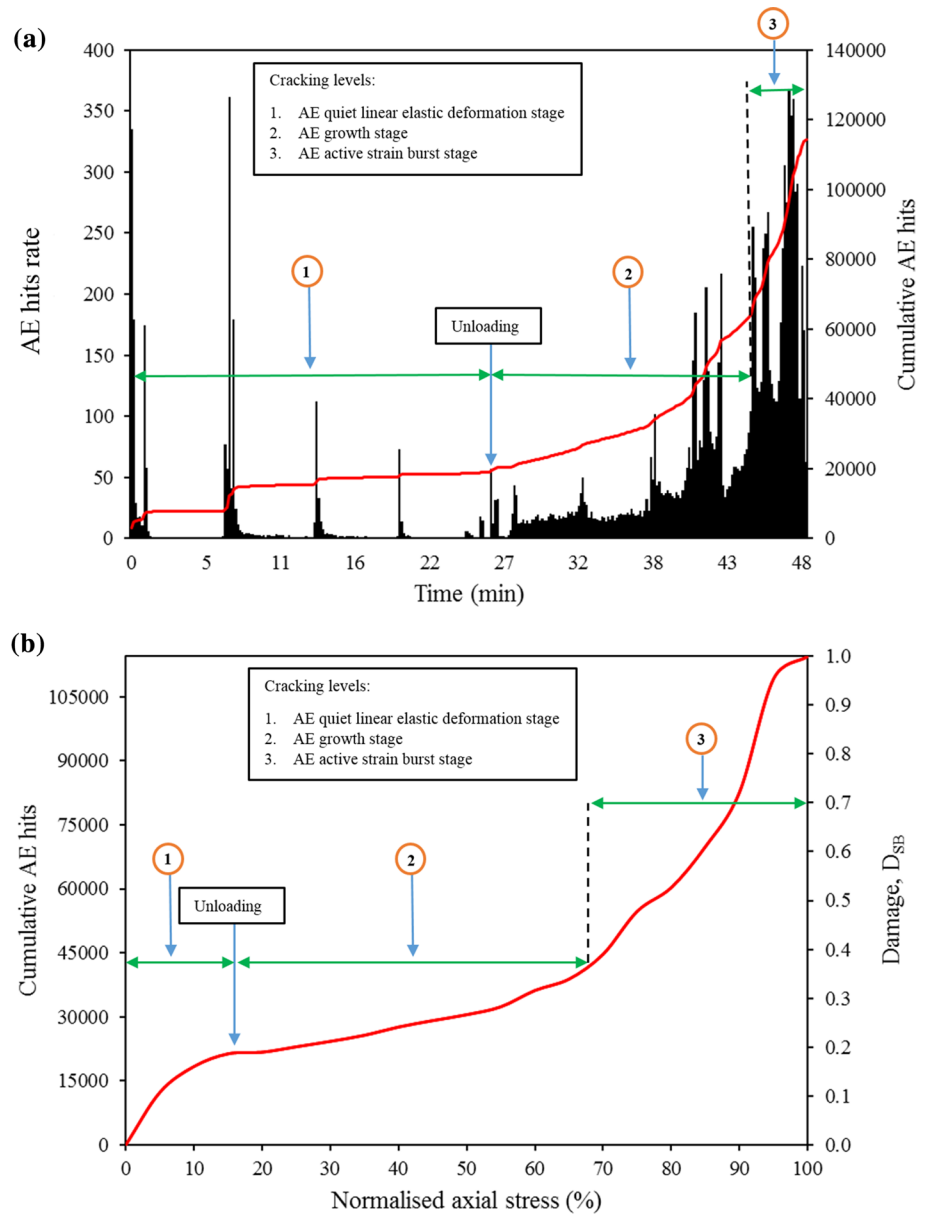


Fig. 11 Plots of **a** AE hits rate and **b** cumulative AE hits and damage evolution by AE hits versus normalised strain burst peak stress at corresponding stages shown in part a for the rock at temperature of 25 °C



$$D_{SB} = \frac{\Omega}{\Omega_m}, \tag{1}$$

where Ω is the cumulative amount of AE energy or number of hits at a certain time during the damage evolution and Ω_m is the cumulative amount of energy or number of hits during the whole testing period. Note that it is also significant that $0 \leq \Omega \leq \Omega_m$ and $0 \leq D_{SB} \leq 1$, in which 0 corresponds to the initial undamaged state of the rock and 1 corresponds to the strain burst.

At the initial stage, a sudden increase can be observed due to the closure of pre-existing cracks, voids or other defects. After the majority of the natural cracks compacted, the rocks went into a linear elastic deformation period. During the stress maintenance phase, the cumulative AE energy rate

changed little indicating that no micro-cracking inside the rocks was observed. During this phase, stiffness started to decrease, and it was associated with signifying tensile or shear movements between the faces of closing or closed cracks (Eberhardt et al. 1998). Upon the unloading of the minimum principal stress σ_3 , the cumulative AE energy gradually increased, revealing that new micro-cracks generated and started to grow. However, their low AE energy indicates that they have limited influence on decreasing the overall strength of the rock and thus cannot cause strain bursting. As the maximum principal stress σ_1 was further increased while intermediate principal stress σ_2 was maintained constant, the micro-cracks began to propagate to a few large cracks, to coalescence and to form macro-cracks. This increasingly contributed to the degradation of the inherent

rock strength, which was revealed by a high amount of cumulative AE energy. At AE active strain burst stage, due to the unstable coalescence of macro-cracks and the ejection of rock fragments from the free face, cumulative AE energy associated with higher amplitudes rapidly increased at a high rate until strain burst occurred. Figure 12 presents variations in the cumulative AE energy and cumulative AE counts with the temperature for all granite specimens. In general, increasing the number of micro-fractures caused a decline in both cumulative AE energy and counts. Nevertheless, as observed in this work, this trend is only correct for sufficiently high temperatures. For example, when the temperatures reached 100 and 150 °C, the cumulative AE energy of the samples decreased by 14–20%, and the cumulative AE counts declined by 20–55%, compared with the values at 25 °C.

The thermal damage influence on strain burst intensity was investigated by estimating the bursting rates. The

evolution of damage was divided into four stages, and the slopes of these stages were calculated (see Fig. 13a). It can be stated that the slope of the damage and cumulative AE energy in the last stage drastically increases the normalised stress level of 90–95%. This is associated with accumulated energy inside the rock. As displayed in Fig. 13b, thermal damage has a significant influence on the damage accumulation rate and on bursting. When the temperature was increased up to 100 °C, the accumulation rate of thermal damage increased. We believe that thermally induced micro-cracks triggered the accumulated damage inside the samples which also influenced the intensity of the strain burst. Therefore, the specimens treated with temperatures from room temperature 25 to 100 °C exhibited less-intense strain bursts due to the rapid damage accumulation (see Fig. 14).

Fig. 12 Influence of temperature on **a** cumulative AE energy, **b** cumulative AE counts

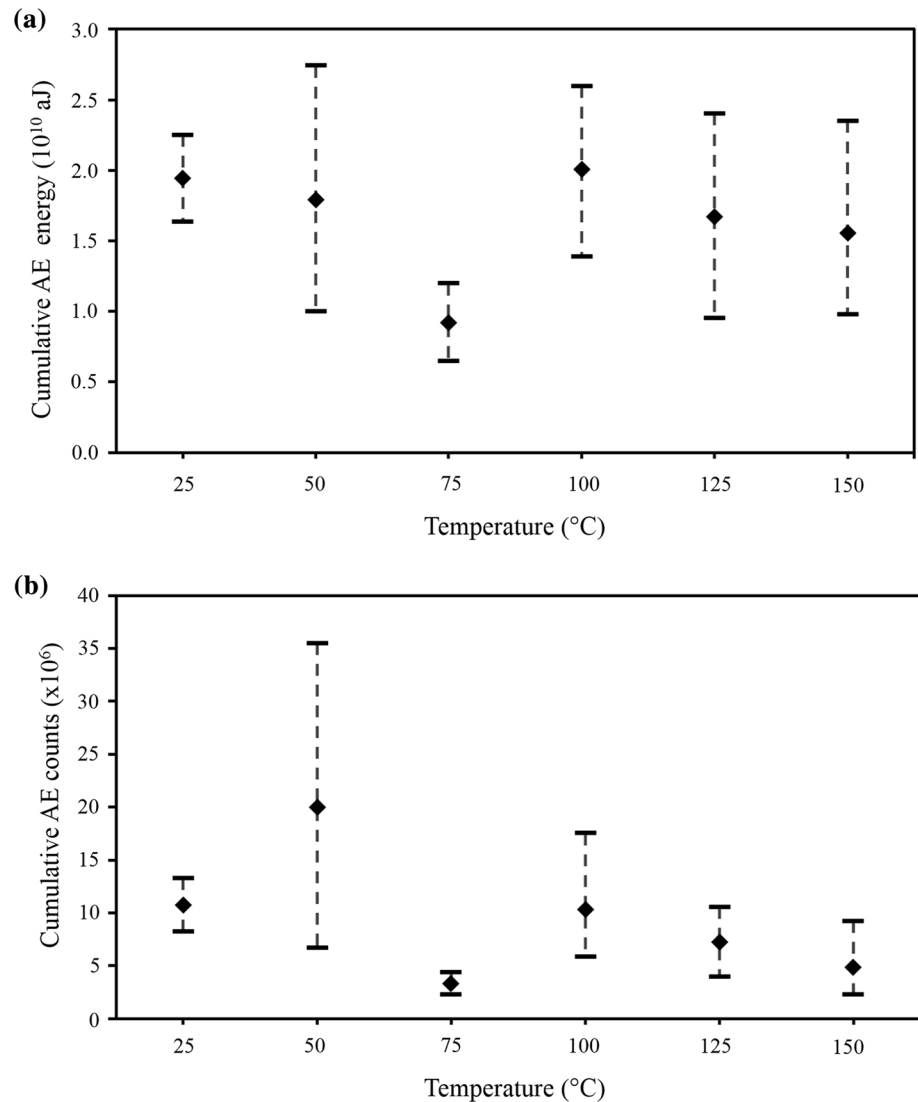


Fig. 13 **a** Slopes of the strain burst damage, D_{SB} , evolution stages, **b** influence of temperature on damage accumulation

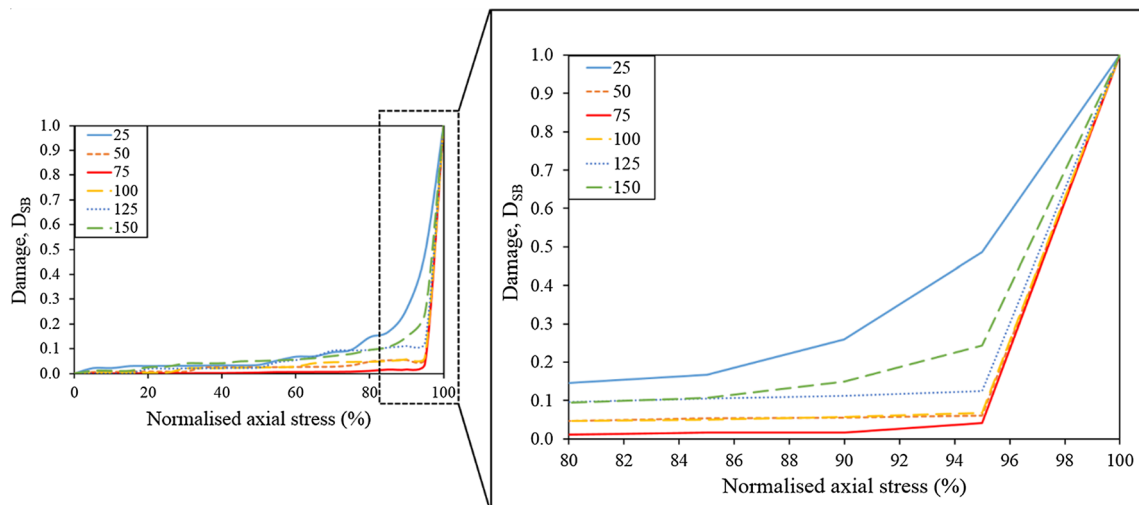
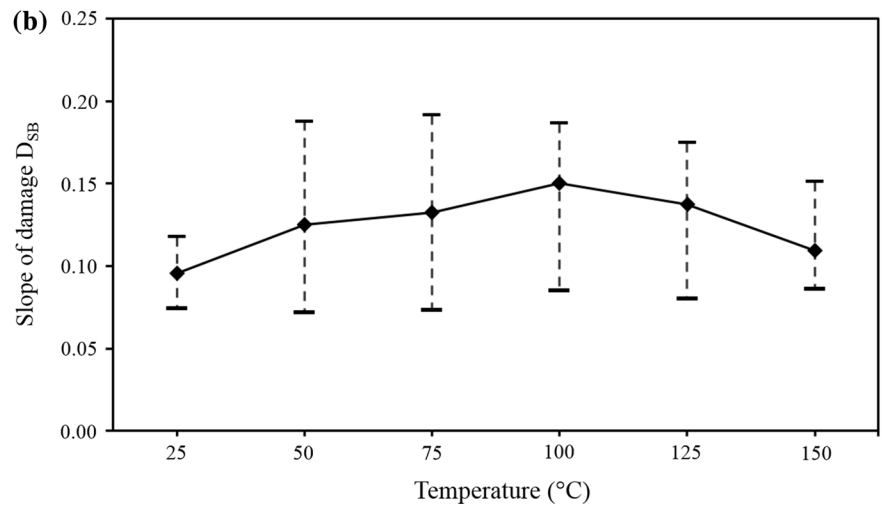
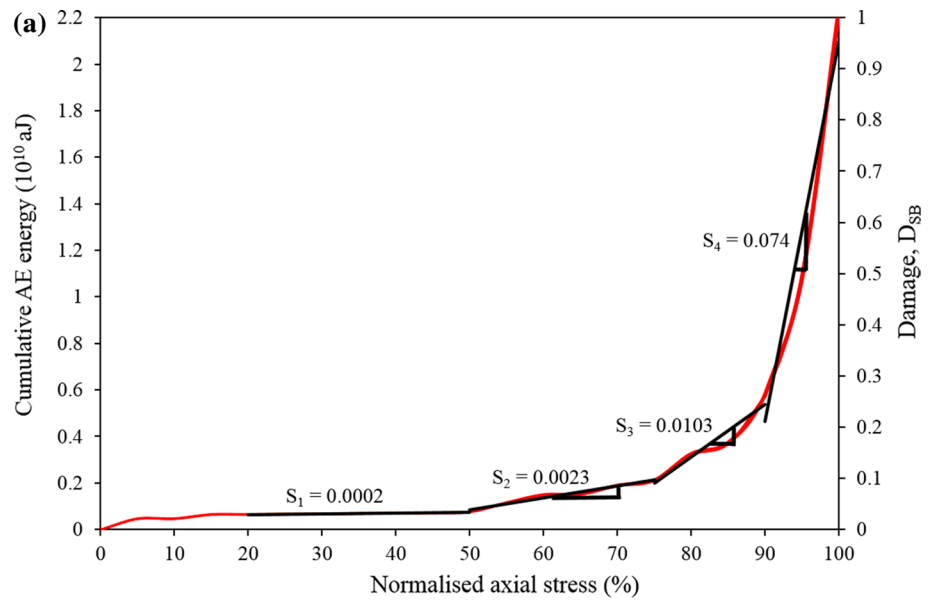


Fig. 14 Thermal damage influence on damage accumulation rate

3.3.2 *b*-Value Analysis

The *b*-value from Gutenberg–Richter's equation (Gutenberg and Richter 1956) has been widely used to assess the internal damage evolution of rock (Grosse and Ohtsu 2008; Carpinteri et al. 2009; Sagar et al. 2012; Kim et al. 2015). The Gutenberg–Richter relation between the cumulative frequency–magnitude distributions of AE data is given in seismology by Eq. 2.

$$\log_{10}(N) = a - b \left(\frac{A_{dB}}{20} \right), \quad (2)$$

where A_{dB} is the peak amplitude of AE events in decibels, N is the incremental frequency which can be defined as the number of AE hits with an amplitude greater than A_{dB} and the *b*-value is the negative slope of the log-linear plot between frequency and amplitude.

For three deformation stages, *b*-values were calculated by plotting the cumulative AE hits, peak amplitude distribution and fitting curve (an example of calculation of *b*-values can be seen in Fig. 15a). Fracture density can be represented by the y-intercept of the fitting line. As can be observed that y-intercepts of the three deformation stages decrease from the initial AE quiet stage to the AE active stage.

Figure 15b presents the estimated *b*-values in three deformation stages. At the initial stage, the closure and compaction of pre-existing micro-cracks, voids or other defects resulted in high *b*-values. This is evidenced by a large number of AE events with low magnitude. During the generation of new micro-cracks, and also during the stable growth of micro-cracks (no macro-crack formation), a few AE events were observed. In the AE active stage, *b*-values decreased sharply. This indicates that AE events with higher amplitudes were detected due to the accelerated unstable crack growth, and coalescence until strain burst. This sudden change in the *b*-value also indicates that the damage accumulated inside the rock is increasing. Therefore, the higher *b*-value trend suggests micro-crack growth, while lower *b*-value trend implies that macro-cracks have formed inside the rock that can be used as a damage alert.

Figure 15c presents the influence of temperature on the *b*-value at AE active stage when the final failure is impending. Carpinteri et al. (2009) indicated that *b*-value changes systematically from 1.5 when the applied load is close to the peak load, to 1.0 when the final failure is imminent, which is characterised by a strong damage localisation. In our tests, we observed that *b*-values shown in Fig. 15c are less than 1.0 at AE active stage. When the temperature increased to 100 °C, *b*-values show an increasing trend. This indicates that thermal damage

reduced the macro-cracking process due to the mechanical degradation of the samples, which in turn resulted in less-intense strain bursting. As the temperature increased from 100 to 150 °C, *b*-values gradually declined which can reveal more intense strain burst characteristics. Therefore, *b*-value analysis can be used to assess the type of deterioration of the rock and to quantify the damage level.

3.3.3 Frequency-Domain Analysis

The frequency–amplitude characteristics of the AE waves of the six granite specimens treated with different temperatures are presented in Fig. 16. The frequency–amplitude behaviours of the AE signals showed trends similar to the total cumulative AE energy responses. Increasing the temperature led to a low-frequency band and higher amplitudes (see Fig. 16). When the frequency–amplitude distribution was higher, significant energy release and intense cracking and bursting evolution were observed. Moreover, the amplitudes gradually increased and reached the maximum values during strain burst except during the initial loading period.

In order to investigate the influence of thermal damage on strain burst behaviours in greater depth, the frequency spectrum analysis was carried out. The AE signals were analysed using the fast Fourier transform (FFT) method (see Eq. 3), as the frequency spectrum can be used to investigate the internal damage level during strain burst.

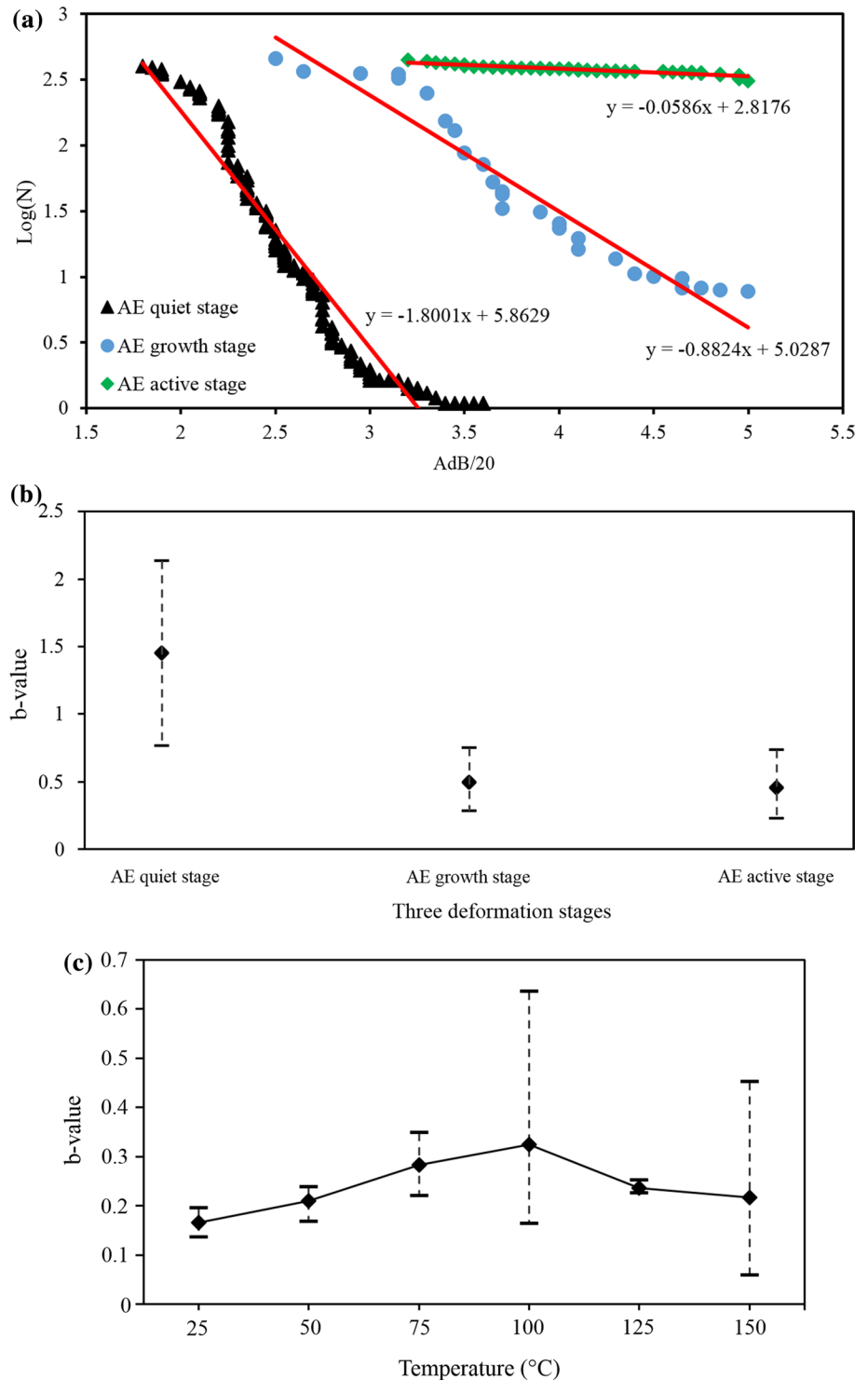
$$X_k = \sum_{n=0}^{N-1} x_n \cdot e^{-i2\pi kn/N} \quad (3)$$

Figure 17 demonstrates the main frequency behaviour when the temperature was increased from room temperature (25 °C) to 150 °C. The average results show that the main frequency was approximately 261 kHz for room temperature samples and continually decreased to around 113 kHz as the temperature was increased. We believe that the micro-cracking processes occurred over a long time period at low temperatures. However, when temperature increased, this micro-cracking period gradually diminished due to the thermal damage inside the specimens.

3.4 Kinetic Energy Analysis for Strain Burst Due to Thermal Damage

The kinetic energy of the rock fragments ejected from the free face of the tested rock specimens can be used as an indicator for quantitatively evaluating the intensity of strain burst. Therefore, calculating the fragment ejection velocities can help us to better understand the energy mechanism of strain burst. A high-speed camera was employed to observe the fragment ejections. The fragment ejection speed was

Fig. 15 Example of calculation of b -values **a** AE incremental frequency and amplitude distribution and b -value calculation, **b** average b -values and standard deviations in three deformation stages for the granite specimen at temperature level of 150 °C, **c** temperature influence on b -value at AE active stage

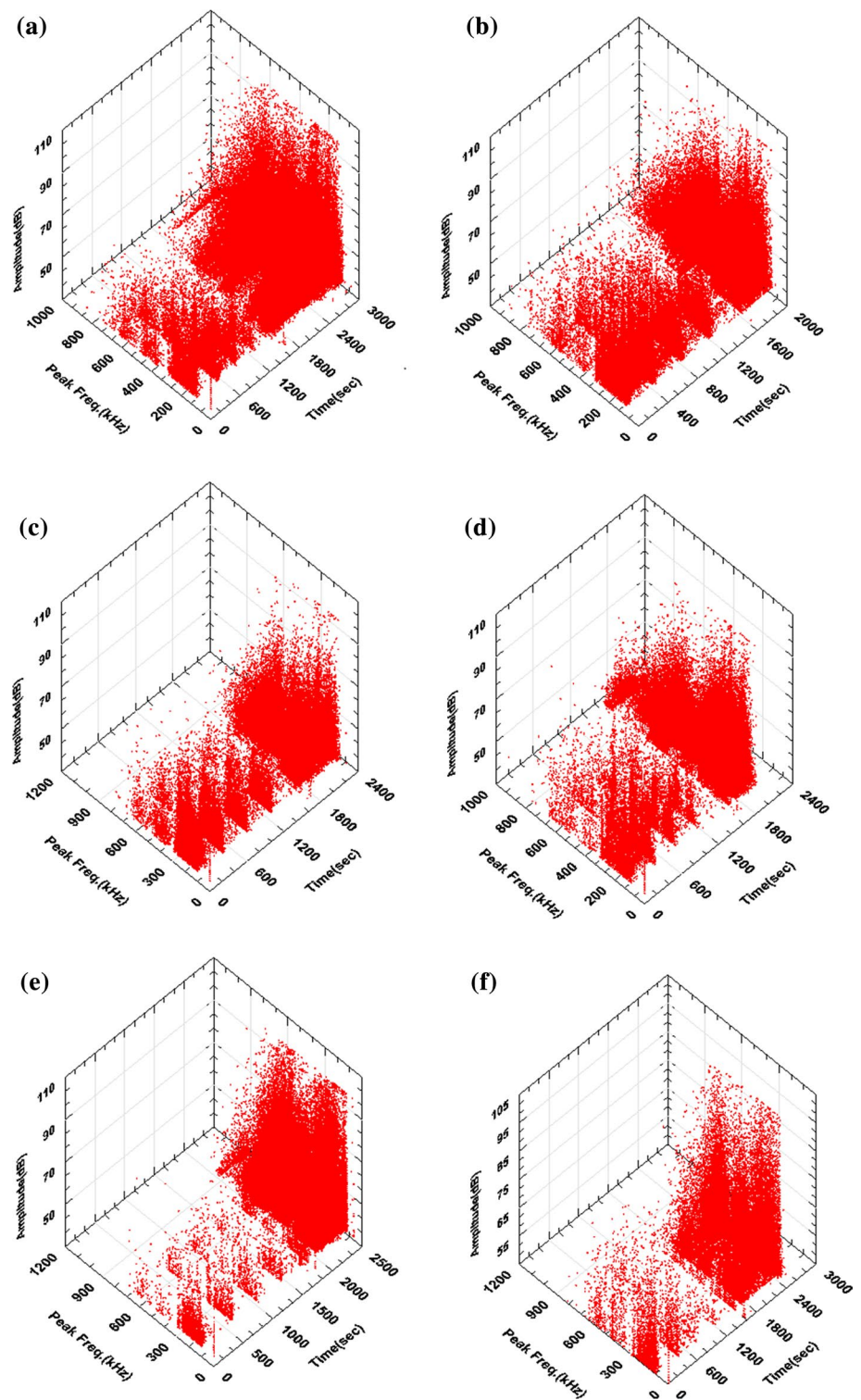


measured by analysing the high-speed videos. The captured images were used to track the movements of the ejected fragments. Note that since the ejected rock fragments are not of uniform size, only fragments with diameters larger than 10 mm and weighing more than 0.5 g were assessed. The granite sample treated with a temperature of 75 °C (B1#4) was taken as an example, and the calculation procedure for

the velocity of the ejected fragments is illustrated in Fig. 18. Figure 18 provides a sketch of the ejected fragment trace, the coordinate system for estimating the location of fragments before and after ejection, a demonstration of a rock fragment and location analysis.

The kinetic energy calculation analysis of the ejected fragments can be described as follows. First, a three-dimensional

Fig. 16 AE frequency–amplitude features of the six granite specimens treated with different temperatures: **a** $T = 25\text{ }^{\circ}\text{C}$, **b** $T = 50\text{ }^{\circ}\text{C}$, **c** $T = 75\text{ }^{\circ}\text{C}$, **d** $T = 100\text{ }^{\circ}\text{C}$, **e** $T = 125\text{ }^{\circ}\text{C}$, **f** $T = 150\text{ }^{\circ}\text{C}$



spatial coordinate system was set up in which the centre bottom of the steel rig was selected as the origin point, denoted by a red circle (see Fig. 18a). Then, the motion trail of relatively large fragments was traced after bursting, as illustrated in Fig. 18b. The specific spatial locations of the fragments were determined from the side view and top view of the

high-speed photographs (see Fig. 18d). Figure 18c presents the movement tracking of the fragment, F-2, from the free face of the granite sample at the onset of bursting to the bottom platform. After calculating the movement time, Δt , locations of the fragments before and after ejection were identified with respect to the spatial coordinate system. As

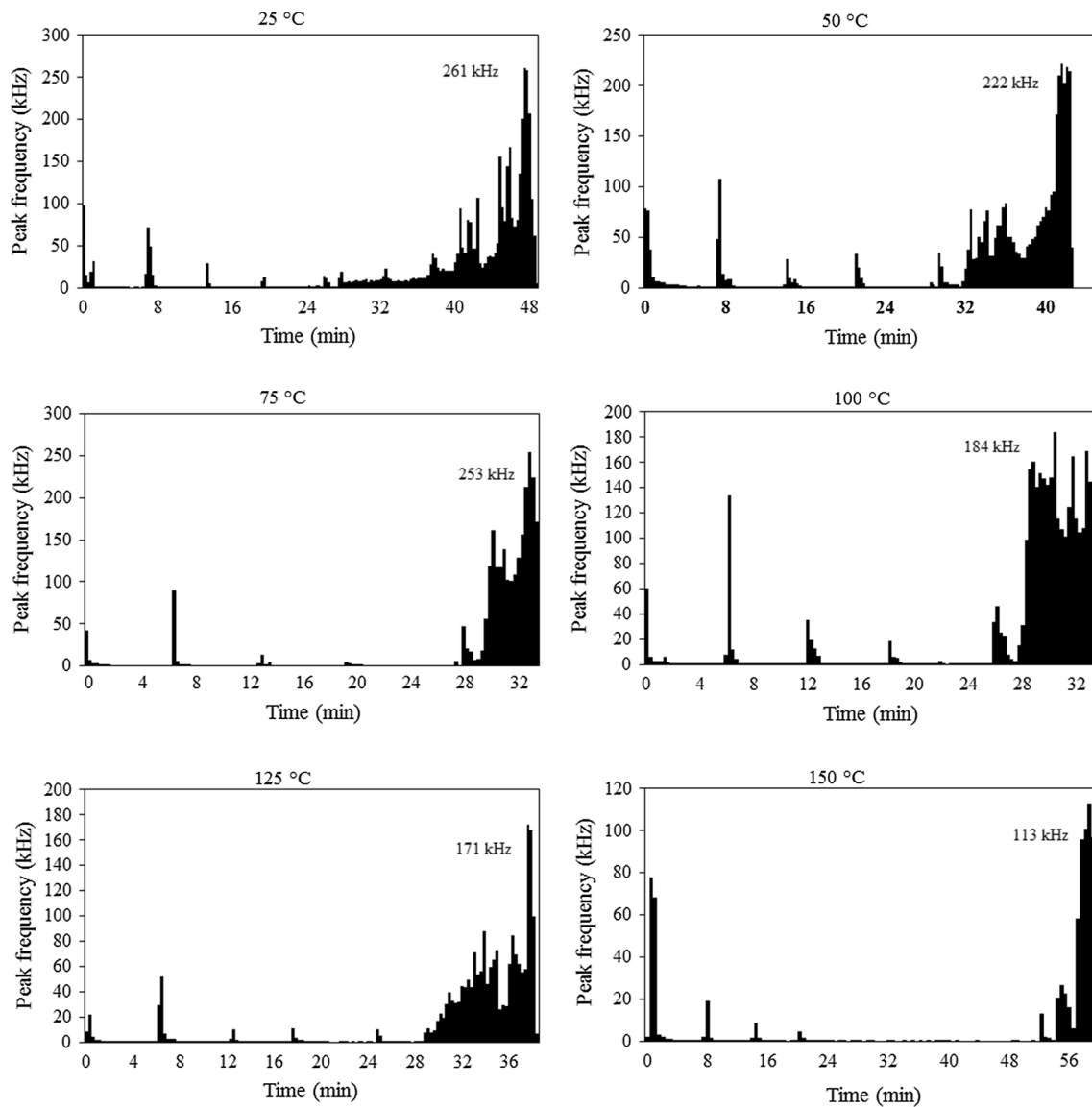


Fig. 17 Influence of temperature on main frequency

can be seen in Fig. 18b, the initial ejection location of the fragment is point A (x_0, y_0, z_0) , which has an initial speed of V_0 and the final dropping down point is point B (x_1, y_1, z_1) .

After measuring the velocity, the total kinetic energy of the ejected fragments was calculated by using Eq. (4):

$$E_k = \sum_{i=1}^n \frac{1}{2} m_i \bar{v}_i^2, \quad (4)$$

where n is the number of fragments having $D > 10$ mm and $m > 0.5$ g, m_i is the mass of the i th rock fragment and \bar{v}_i is the initial ejection velocity of the i th rock fragment. By using the equation above, we calculated the total kinetic energies for all granite specimens treated with different temperatures. Note that average velocity values of the

ejected fragments were taken as the ejection velocity of a granite specimen. The ejection velocities and strain bursting of the granite specimens exposed to different temperature conditions from room temperature (25 °C) to 150 °C are displayed in Fig. 19. Due to the thermal damage occurred inside the granite samples leading to the degradation of the mechanical characteristics, the ejection velocity of the fragments dramatically decreased when the temperature level was below 100 °C. With improved compactness between 100 and 150 °C, the velocity of the ejected fragments increased slightly, which is associated with relatively intense strain bursting (see Fig. 20a).

The kinetic energy of the ejected fragments showed a trend similar to the ejection velocities. Kinetic energy continually decreased with the temperature, until the critical

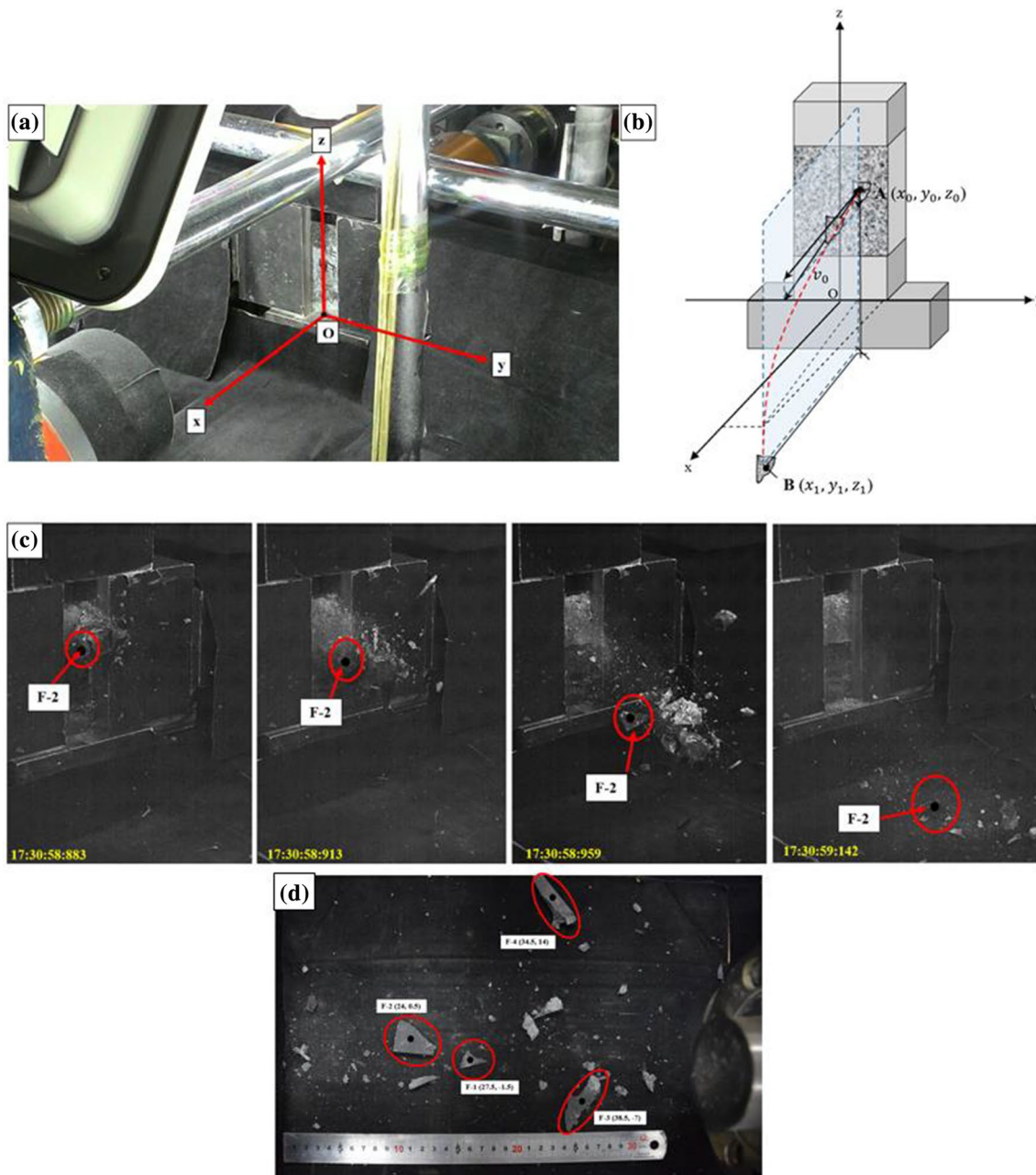


Fig. 18 **a** Fragment coordinate information system, **b** sketch of the ejected fragment trace, **c** high-speed camera images of the ejected fragment (the numbers at the bottom-left corner of the images denote the time in h:m:s:ms and **d** location analysis of the ejected fragments

temperature level of 100 °C was reached. This is because the granite specimens manifested thermal damage (see Fig. 20b). The strain burst stress and total elastic strain energy showed a decline in temperatures below 100 °C due to thermally induced damage and are shown in Fig. 20a. It can also be seen that the amount of total elastic strain energy released from the granite specimens decreased because the thermally induced micro-cracks reduced the amount of strain energy accumulation (see Fig. 21b). When the temperature increased from 100 to 150 °C, the accumulated

strain energy within the granite specimens increased (see Fig. 21a). Therefore, this led to the higher amount of the strain energy release associated with an increase in kinetic energy, as shown in Fig. 20a.

Table 4 presents the changes in strain burst stress, accumulated total elastic strain energy, released kinetic energy and the velocity of the ejected fragments. In general, the higher the strain burst stress, the higher the total elastic strain energy, with greater energy release and thus higher kinetic energy levels. When the temperature increased

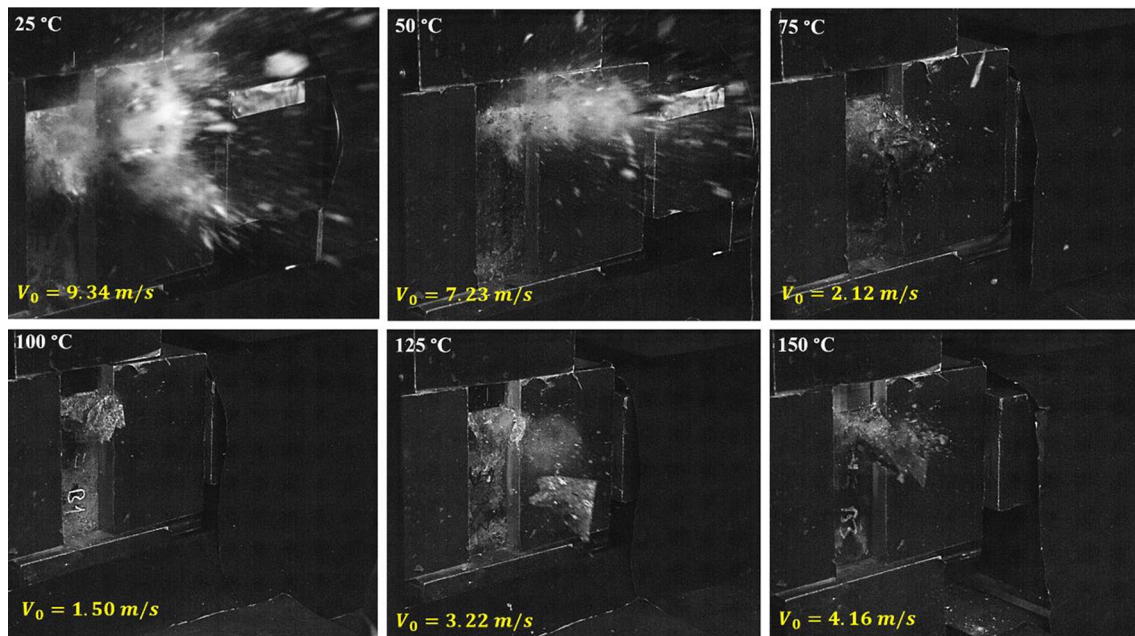


Fig. 19 Ejection velocities of rock fragments from the granite specimens treated with different temperature conditions

from room temperature (25 °C) to the critical temperature level (100 °C), strain burst stress, total elastic strain energy, kinetic energy and the ejection velocity of the fragments decreased by 45, 68, 96 and 82%, respectively. We believe that thermally induced micro-cracking caused mechanical degradation and this resulted in less strain energy accumulation, which led to small kinetic energy. When the temperature level was above 100 °C, bursting stress, accumulated strain energy, kinetic energy release and fragment ejection velocity increased when compared to the results captured at the temperature of 100 °C. This led to more intense strain burst characteristics. The results demonstrate that thermal damage has some influence on strain burst behaviour of brittle rock.

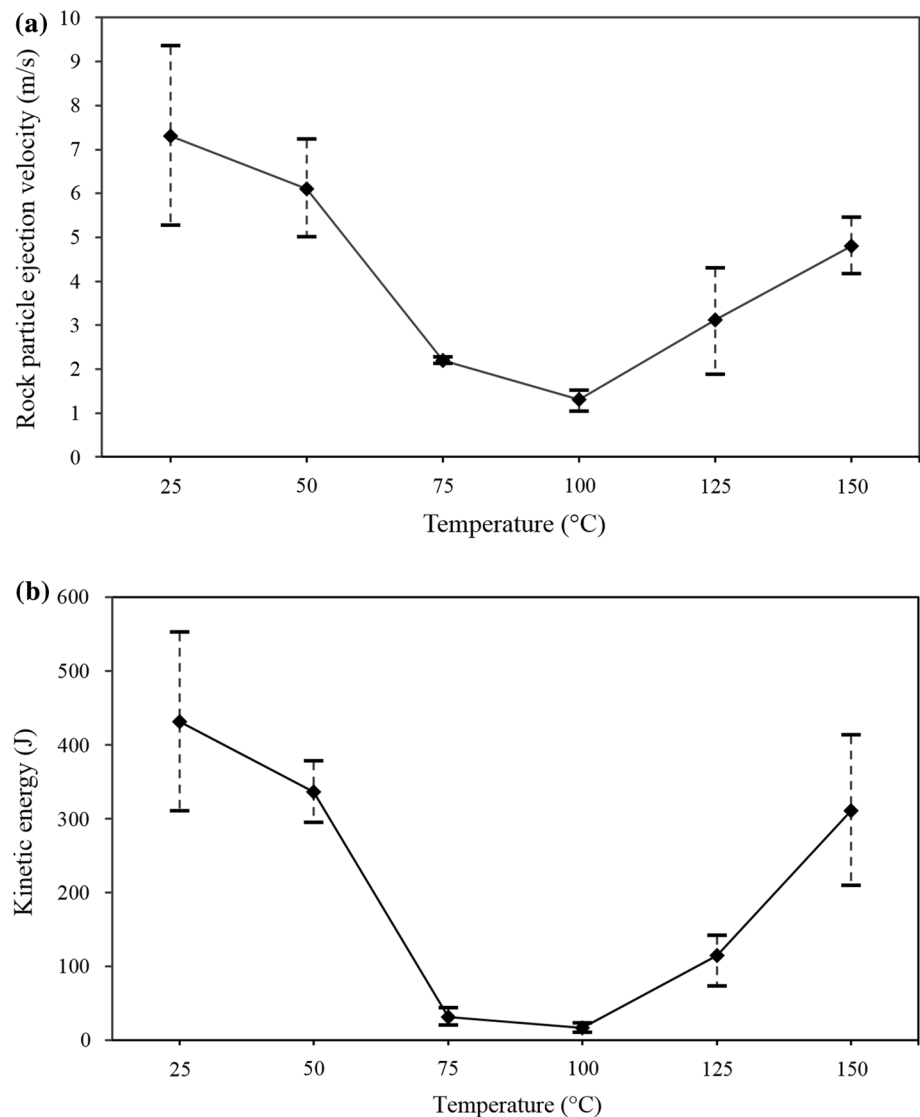
4 Discussions

Strain burst stresses for the samples exposed to temperatures up to 100 °C declined by 44.6%, compared to the stresses of the specimens at the room temperature (25 °C) (see Fig. 8). We believe that creation of new micro-cracks due to temperature exposure led to a weakening of the bonding among mineral grains of the samples, which can be attributed to the anisotropy in the thermodynamic properties of different rock minerals, and this caused a degradation of the overall rock strength. The failure mechanism for the granite specimens exposed to temperatures up to 100 °C might have been due to intergranular fracture mechanism in which micro-cracks first develop at the mineral grain boundaries that was

consistent with the existing literature (Yin et al. 2012; Zuo et al. 2014; Li et al. 2016; Feng et al. 2017). As the temperature increased from 100 up to 150 °C, the strain burst stress showed a gradual rise. It is believed that the closure of pre-existing micro-cracks due to the thermal expansion of mineral grains by high temperature may render the rocks denser and more compact (Funatsu et al. 2014; Gautam et al. 2016). In order to understand this phenomenon, SEM analysis needs to be conducted, which is a subject of our future work. However, experimental evidence in the literature suggests that the above-mentioned mechanisms of intergranular and transgranular thermal cracking could be behind the observed behaviour in this study. In fact, Zuo et al. (2014) and Feng et al. (2017) reported that when the temperature was more than 100 °C, the coupled fracture mechanism of intergranular and transgranular thermal cracking (in which the micro-cracks develop within the mineral grains) was the main mechanism for improved compactness of the specimens after the gradual closure of the pre-existing defects in the crystal.

Since the effects of the micro-cracking process are related to the magnitude of the AE events, damage evaluation will be better understood with cumulative AE energy. It was observed that the rate of thermal damage accumulation increased as the temperature increased from room temperature (25 °C) up to 100 °C. We believe that the weakening of the minerals' bonding caused a mechanical degradation on the strength of the rocks and this triggered the rapid thermal damage accumulation and bursting. On the other hand, when the temperature increased from 100

Fig. 20 Ejection velocity and kinetic energy of the granite specimens treated with different temperature conditions



to 150 °C, the granite specimens exhibited slower damage accumulation and revealed intense strain burst. This can be attributed to the improved densification of the samples due to the thermal dilation of mineral grains which decreased the distance between the interfaces of the minerals, and their mutual attraction was enhanced.

From an energy point of view, kinetic energies of the granite specimens were calculated to assess the influence of thermal damage on the intensity of strain burst. The samples treated with temperatures from room temperature (25 °C) to 100 °C manifested dramatically less-intense strain burst associated with slower particle ejection velocities due to the thermal damage. At temperatures from 100 to 150 °C, more intense strain burst was displayed with faster rock fragment ejection. It is believed that this increase in kinetic energy was caused by the enhanced compactness of the samples due to the fact that thermally induced volumetric expansion of minerals led to

the closure of the pre-existing micro-cracks and original defects in the samples.

The aforementioned experimental results give useful enlightenments about the impact of thermal damage on strain burst characteristics. However, more experiments considering higher temperature levels should be performed to better understand the mechanism of strain burst under high geo-stress and high-temperature conditions.

5 Conclusion

In this study, temperature influence on the strain burst behaviour of granite samples was investigated using a unique true-triaxial strain burst testing system. Based on acoustic emission, stress and kinetic energy analyses on the granite samples, which were exposed to various temperatures, the following conclusions can be drawn:

Fig. 21 Total elastic strain energy and amount of released elastic strain energy with respect to different temperature levels

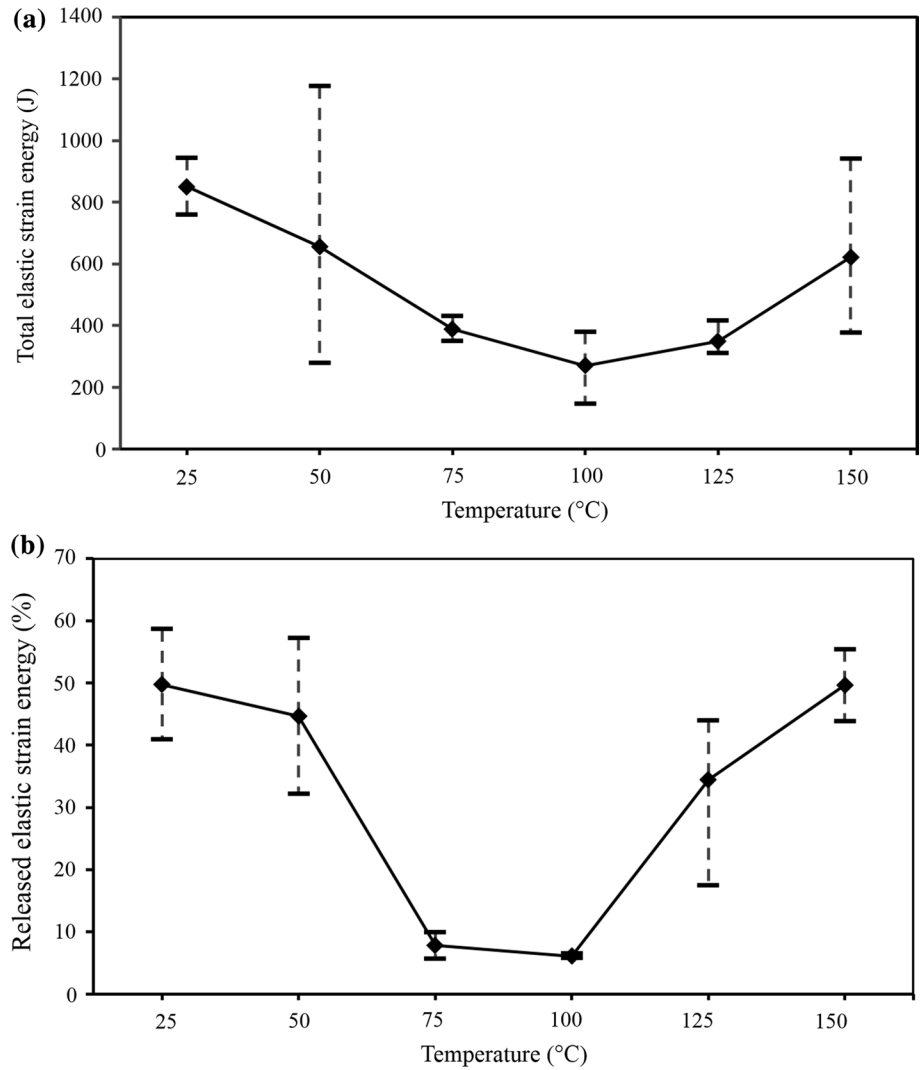


Table 4 Temperature influence on strain burst stress, total elastic strain energy, kinetic energy and ejection velocity of the fragments

Temperature (°C)	25	50	75	100	125	150
Strain burst stress (%)	0	- 15.7	- 32.2	- 44.6	- 35.9	- 15.8
Total elastic strain energy (%)	0	- 22.9	- 54.1	- 68.2	- 58.9	- 26.9
Kinetic energy (%)	0	- 22.1	- 92.8	- 96.3	- 73.4	- 27.9
Ejection velocity of the fragments (%)	0	- 16.3	- 70.0	- 82.0	- 57.2	- 34.3

1. The strain burst stress of granite changes with temperature from room temperature (25 °C) to 150 °C. A temperature level of 100 °C was identified as the critical transition temperature, which induces the change in the strain burst behaviours of granite. As the temperature increased from 25 to 100 °C, the strain burst stress diminished by approximately 45%. We believe that this declining trend is caused by the development of micro-cracks that are induced by temperatures. At 100–150 °C, the strain burst stress showed a slightly rising trend, but it is still less than that at room temperature. This can be

attributed to the improved compaction of the grains in brittle rock by the closure of pre-existing micro-cracks due to the thermal expansion of minerals at higher temperatures.

2. The evolution of AE characteristics can be divided into three deformation stages. Those stages are the AE quiet linear elastic deformation stage, AE growth stage and AE active strain burst stage. The cumulative AE energy showed a sharp increase at the initial stage and then accumulated slowly during the stress maintenance phase before increasing dramatically until strain burst

occurred. Corresponding with the failure characteristics of the granite specimens exposed to different temperature conditions, the total cumulative AE energy and cumulative AE counts decreased as the temperature increased from 100 to 150 °C. It was found that cumulative AE energy characteristics reflect the damage evolution better as the size of micro-cracks is related to the magnitude of the AE events. Moreover, when the temperature increased, a low-frequency band was observed due to the thermal damage inside the specimens, which can also be an indicator for strain burst.

3. The thermal damage for strain burst (D_{SB}) increased the rate of bursting at ~ 95% of normalised axial stress levels. This can be due to thermally induced micro-cracks that helped to reduce the accumulated energy at the initial loading stage. A good relationship was observed between the trend of the b -values and the micro- and macro-cracking during the strain burst test. The estimated b -values showed a continuously declining trend during the test indicating that a large amount of macro-cracks were generated prior to strain burst. Therefore, b -value analysis can be used as a precursor to assess the degradation of the rock and strain burst process.
4. The kinetic energy of the ejected fragments dramatically decreased until they reached the critical temperature of 100 °C. This is because of manifested thermally induced damage, which caused less elastic strain energy accumulation. When the temperature increased from 100 to 150 °C, kinetic energy had also a slight rise, which is associated with the higher initial velocity of ejected fragments which may occur due to the expansion of mineral grains by increased temperature. This helped to improve the compactness of the rock, which implies that a more intense or severe strain burst may be encountered in situations where temperatures rise above the critical temperature of 100 °C.

The results of this study demonstrate that thermally induced damage can change strain burst characteristics of brittle rocks.

Acknowledgements The authors gratefully acknowledge the financial support from the Australian Research Council (ARC-LP150100539), OZ Minerals and the principal geotechnical manager, David Goodchild. The authors also thank Adam Rytjes for his valuable help in the specimen preparation. Leticia Mooney is acknowledged for her English editing.

References

- Akdag S, Karakus M, Nguyen GD, Taheri A (2017) Influence of specimen dimensions on bursting behaviour of rocks under true-triaxial loading conditions. In: Wesseloo J (ed) 8th International conference on deep and high stress mining. Australian Centre for Geomechanics, Perth, pp 447–457
- Aoki H, Matsukara Y (2008) Estimating the unconfined compressive strength of intact rocks from Equotip hardness. *Bull Eng Geol Environ* 67(1):23–29
- Atkinson R, Ko H (1973) A fluid cushion, multiaxial cell for testing cubical rock specimens. *Int J Rock Mech Min Sci Geomech Abstr* 10:351–361
- Cai M (2008) Influence of stress path on tunnel excavation response—numerical tool selection and modeling strategy. *Tunn Undergr Sp Technol* 23:618–628
- Carpinteri A, Lacidogna G, Puzzi S (2009) From criticality to final collapse: evolution of the “ b -value” from 1.5 to 1.0. *Chaos Soliton Frac* 41:843–853
- Carpinteri A, Lacidogna G, Accornero F, Mpalaskas AC, Matikas TE, Aggelis D (2013) Influence of damage in the acoustic emission parameters. *Cem Concr Compos* 44:9–16
- Chen Y, Ni J, Shao W, Azzam R (2012) Experimental study on the influence of temperature on the mechanical properties of granite under uni-axial compression and fatigue loading. *Int J Rock Mech Min Sci* 56:62–66
- Coli M, Livi E, Berry P, Bandini A, Jia XN (2010) Studies for rock-burst prediction in the Carrara marble (Italy). In: Xie F (ed) *Proceeding of the 5th international symposium on in-situ rock stress*. CRC Press, Beijing, pp 367–373
- Ding Q, Ju F, Mao X, Ma D, Yu B, Song S (2016) Experimental investigation of the mechanical behavior in unloading conditions of sandstone after high temperature treatment. *Rock Mech Rock Eng* 49:2641–2653
- Dwivedi R, Goel R, Prasad V, Sinha A (2008) Thermo-mechanical properties of Indian and other granites. *Int J Rock Mech Min Sci* 45:303–315
- Eberhardt E, Stead D, Stimpson B, Read R (1998) Identifying crack initiation and propagation thresholds in brittle rock. *Can Geotech J* 35(2):222–233
- Fairhurst C, Hudson J (1999) Draft ISRM suggested method for the complete stress-strain curve for intact rock in uniaxial compression. *Int J Rock Mech Min Sci* 36:279–289
- Feng G, Feng X, Chen B, Xiao Y, Yu Y (2015) A microseismic method for dynamic warning of rockburst development processes in tunnels. *Rock Mech Rock Eng* 48:2061–2076
- Feng X, Zhang X, Kong R, Wang G (2016) A novel mogi type true triaxial testing apparatus and its use to obtain complete stress-strain curves of hard rocks. *Rock Mech Rock Eng* 49:1649–1662
- Feng G, Kang Y, Meng T, Hu Y, Li X (2017) The influence of temperature on mode I fracture toughness and fracture characteristics of sandstone. *Rock Mech Rock Eng* 50:2007–2019
- Funatsu T, Kuruppu M, Matsui K (2014) Effects of temperature and confining pressure on mixed-mode (I-II) and mode II fracture toughness of Kimachi sandstone. *Int J Rock Mech Min Sci* 67:1–8
- Gautam P, Verma A, Maheshwar S, Singh T (2016) Thermomechanical analysis of different types of sandstone at elevated temperature. *Rock Mech Rock Eng* 49:1985–1993
- Gong Q, Yin L, Wu S, Zhao J, Ting Y (2012) Rock burst and slabbing failure and its influence on TBM excavation at headrace tunnels in Jinping II hydropower station. *Eng Geol* 124:98–108
- Grosse C, Ohtsu M (2008) *Acoustic emission testing*. Springer, Berlin
- Gutenberg B, Richter C (1956) Magnitude and energy of earthquakes. *Ann Geophys* 9(1):1–15
- Haimson B, Chang C (2000) A new true triaxial cell for testing mechanical properties of rock, and its use to determine rock strength and deformability of Westerly granite. *Int J Rock Mech Min Sci* 37:285–296
- He M, Miao J, Feng J (2010) Rock burst process of limestone and its acoustic emission characteristics under true-triaxial unloading conditions. *Int J Rock Mech Min Sci* 47:286–298

- He M, Jia X, Coli M, Livi E, Sousa L (2012) Experimental study of rockbursts in underground quarrying of Carrara marble. *Int J Rock Mech Min Sci* 52:1–8
- He B, Zelig R, Hatzor Y, Feng X (2016) Rockburst generation in discontinuous rock masses. *Rock Mech Rock Eng* 49:1–22
- Hedley D (1992) Rockburst handbook for Ontario hardrock mines. CANMET Special Report
- Heuze F (1983) High-temperature mechanical, physical and thermal properties of granitic rocks—a review. *Int J Rock Mech Min Sci* 20(1):3–10
- Hua A, You M (2001) Rock failure due to energy release during unloading and application to underground rock burst control. *Tunn Undergr Sp Technol* 16:241–246
- Huang R, Wang X, Chan L (2001) Triaxial unloading test of rocks and its implication for rock burst. *Bull Eng Geol Env* 60:37–41
- Karakus M, Akdag S, Bruning T (2016) Rock fatigue damage assessment by acoustic emission. In: Ranjith P, Zhao J (ed) International conference on geo-mechanics, geo-energy and geo-resources, *IC3G*, (pp. 9–82–88). Melbourne, Australia
- Kim J, Lee K, Cho W, Choi H, Cho G (2015) A comparative evaluation of stress-strain and acoustic emission methods for quantitative damage assessments of brittle rock. *Rock Mech Rock Eng* 48:495–508
- Kong B, Wang E, Li Z, Wang X, Liu J, Li N (2016) Fracture mechanical behavior of sandstone subjected to high-temperature treatment and its acoustic emission characteristics under uniaxial compression conditions. *Rock Mech Rock Eng* 49:4911–4918
- Kumari WGP, Ranjith PG, Perera MSA, Chen BK, Abdulagatov IM (2017) Temperature-dependent mechanical behaviour of Australian Strathbogie granite with different cooling treatments. *Eng Geol* 229:31–44
- Li S, Feng X, Li Z, Chen B, Zhang C, Zhou H (2012) In situ monitoring of rockburst nucleation and evolution in the deeply buried tunnels of Jinping II hydropower station. *Eng Geol* 137–138:85–96
- Li X, Du K, Li D (2015) True triaxial strength and failure modes of cubic rock specimens with unloading the minor principal stress. *Rock Mech Rock Eng* 48:2185–2196
- Li M, Mao X, Cao L, Pu H, Mao R (2016) Effects of thermal treatment on the dynamic mechanical properties of coal measures sandstone. *Rock Mech Rock Eng* 49:3525–3539
- Liu S, Xu J (2013) Study on dynamic characteristics of marble under impact loading and high temperature. *Int J Rock Mech Min Sci* 62:51–58
- Lockner D (1993) The role of acoustic emission in the study of rock fracture. *Int J Rock Mech Min Sci Geomech Abstr* 30:883–899
- Masri M, Sibai M, Shao J, Mainguy M (2014) Experimental investigation of the effect of temperature on the mechanical behavior of Tournemire shale. *Int J Rock Mech Min Sci* 70:185–191
- Michelis P (1985) A true triaxial cell for low and high pressure experiments. *Int J Rock Mech Min Sci Geomech Abstr* 22(3):183–188
- Mogi K (1971) Fracture and flow of rocks under high triaxial compression. *J Geophys Res* 76(5):1255–1269
- Mohamadi M, Wan R (2016) Strength and post-peak response of Colorado shale at high pressure and temperature. *Int J Rock Mech Min Sci* 84:34–46
- Nasseri M, Goodfellow S, Lombo L, Young R (2014) 3-D transport and acoustic properties of Fontainebleau sandstone during true-triaxial deformation experiments. *Int J Rock Mech Min Sci* 69:1–18
- Nemat-Nasser S, Horii H (1982) Compression-induced nonplanar crack extension with application to splitting, exfoliation and rockburst. *J Geophys Res* 87:6805–6821
- Nicksiar M, Martin C (2012) Evaluation of methods for determining crack initiation in compression tests on low-porosity rocks. *Rock Mech Rock Eng* 45:607–617
- Sagar R, Prasad B, Kumar S (2012) An experimental study on cracking evolution in concrete and cement mortar by the b-value analysis of acoustic emission technique. *Cem Concr Res* 42:1094–1104
- Sirdesai N, Singh T, Ranjith P, Singh R (2017) Effect of varied durations of thermal treatment on the tensile strength of red sandstone. *Rock Mech Rock Eng* 50:205–213
- Su G, Jiang J, Zhai S, Zhang G (2017) Influence of tunnel axis stress on strainburst: an experimental study. *Rock Mech Rock Eng* 50:1551–1567
- Sun Q, Zhang W, Xue L, Zhang Z, Su T (2015) Thermal damage pattern and thresholds of granite. *Environ Earth Sci* 74:2341–2349
- Takahashi M, Koide H (1989) Effect of the intermediate principal stress on strength and deformation behavior of sedimentary rocks at the depth shallower than 2000 m. *ISRM International symposium. International Society for Rock Mechanics, Pau*, pp 19–26
- Wang J, Park H (2001) Comprehensive prediction of rockburst based on analysis of strain energy in rocks. *Tunn Undergr Sp Technol* 16(1):49–57
- Wawersik W, Carlson L, Holcomb D, Williams R (1997) New method for true-triaxial rock testing. *Int J Rock Mech Min Sci* 34:330–344
- Xu XL, Karakus M (2018) A coupled thermo-mechanical damage model for granite. *Int J Rock Mech Min Sci* 103:195–204
- Yao M, Rong G, Zhou C, Peng J (2016) Effects of thermal damage and confining pressure on the mechanical properties of coarse marble. *Rock Mech Rock Eng* 49:2043–2054
- Yin T, Li X, Xia K, Huang S (2012) Effect of thermal treatment on the dynamic fracture toughness of Laurentian granite. *Rock Mech Rock Eng* 45:1087–1094
- Zhang C, Feng X, Zhou H, Qiu S, Wu W (2012) Case histories of four extremely intense rockbursts in deep tunnels. *Rock Mech Rock Eng* 45:275–288
- Zhao X, Cai M (2014) Influence of specimen height-to-width ratio on the strainburst characteristics of Tianhu granite under true-triaxial unloading conditions. *Can Geotech J* 52:890–902
- Zhao X, Wang J, Cai M, Cheng C, Ma L, Su R, Li D (2014) Influence of unloading rate on the strainburst characteristics of Beishan granite under true-triaxial unloading conditions. *Rock Mech Rock Eng* 47:467–483
- Zhao X, Cai M, Wang J, Li P (2015) Objective determination of crack initiation stress of brittle rocks under compression using AE measurement. *Rock Mech Rock Eng* 48:2473–2484
- Zuo J, Xie H, Dai F, Ju Y (2014) Three-point bending test investigation of the fracture behavior of siltstone after thermal treatment. *Int J Rock Mech Min Sci* 70:133–143